Available online at www.sciencedirect.com

ScienceDirect

MATTER AND RADIATION AT EXTREMES

Matter and Radiation at Extremes 1 (2016) 277–307

www.journals.elsevier.com/matter-and-radiation-at-extremes

Review Article

Ion stopping in dense plasmas: A basic physics approach

Claude Deutsch*, Gilles Maynard

Laboratoire de Physique des Gaz et Plasmas, CNRS, Univ-Paris Sud, Université Paris-Saclay, 91405 Orsay, France

Received 1 June 2016; revised 21 September 2016; accepted 13 October 2016
Available online 2 December 2016

Abstract

We survey quite extensively the present research status of ion-stopping in dense plasmas of potential importance for initial confinement fusion (ICF) driven by intense and heavy ion beams, and also for warm dense matter (WDM). First, we put emphasis on every possible mechanism involved in the shaping of the ion projectile effective charge, while losing energy in a target plasma with classical ions and partially degenerate electrons.

Then, we switch to ion stopping by target bound electrons, taking detailed account of mean excitation energies. Free electron stopping has already been given a lot of attention in former works [C. Deutsch et al., *Recent Res. Devel. Plasma* 1 (2000) 1–23; *Open Plasma Phys. J.* 3 (2010) 88–115]. Then, we extend the usual standard stopping model (SSM) framework to nonlinear stopping including a treatment of the Z^3 Barkas effect and a confronting comparison of Bloch and Bohr Coulomb logarithms.

Finally, we document low velocity ion slowing down (LVISD) in single ion plasmas as well as in binary ionic mixtures (BIM), in connection with specific ICF fuels.

PACS Codes: 52.50.Gj; 34.50.Bw; 34.50.Fa; 34.80.Lx; 52.27.Gr; 52.27.cm

Keywords: Ion projectile effective charge; Mean excited energies; Nonlinear stopping; Binary ionic mixture

General considerations

Non-relativistic stopping of point like charges in a dense electron fluid has provided us with a fundamentally robust as well as highly versatile paradigm elaborated through a dielectic formulation. So, it thus appears possible to envision now a higher level of complexity in our model approach. The conceptual framework previously developed could also allow for a quantitative treatment of additional basic features of ion-plasma interaction. Those include in-flight balance of the projectile effective charge $Z_{\mathrm{eff}}(V_{\mathrm{p}})$, stopping by electrons bound in the target, or the finite extension (non-punctuality) of the projectile ion electron distribution. The corresponding and suitably extended stopping theory could then be expected to be of quantitative accuracy in modeling the penetration of multi-charged and non-relativistic ions in a small spherical pellet containing a thermonuclear deuterium + tritium (DT) fuel.

Through the remaining electrons bound to the target ions are now directly taking part in the stopping process of the incoming projectile.

These contentions may be given an immediate content by focusing our attention on a high temperature target. Then, the ion projectile-target electron coupling may be considered in the well-known Coulomb logarithm approximation. An obvious extension of the previous standard stopping model (SSM), may thus be written as

$$-\frac{\mathrm{d}E}{\mathrm{d}x}=\frac{4\pi N_0 e^4}{A_{\mathrm{T}} m_{\mathrm{e}} V_{\mathrm{p}}^2}\rho Z_{\mathrm{eff}}^2(V_{\mathrm{p}})(Z_{\mathrm{T}}-\overline{Z})\ln\Lambda_{\mathrm{B}}+ZG(V/V_{\mathrm{e}})\ln\Lambda_{\mathrm{F}}+[\mathrm{ions}], \tag{1}$$

with $G(X)\to 1$ for $V_{\mathrm{p}}\gg V_{\mathrm{the}}$, $G(X)\to 0$ as $(V_{\mathrm{p}}/V_{\mathrm{the}})^3$,

* Corresponding author.
E-mail address: claude.deutsch@u-psud.fr (C. Deutsch).

Peer review under responsibility of Science and Technology Information Center, China Academy of Engineering Physics.

http://dx.doi.org/10.1016/j.mre.2016.11.004

V_{the} = electron thermal velocity
ρ = target density (g/cm^3)
N_0 = Avogadro number
I = mean excitation energy of target bound electrons

$$\text{with } \Lambda_B = \frac{2m_e V_p^2}{I} \text{ and } \Lambda_F = \frac{2m_e V_p^2}{\hbar\omega_p}. \tag{2}$$

For instance, at $n_e \approx 10^{23}$ cm^{-3} and 100 eV one has $\omega_p \approx 2 \times 10^{16}$/s, $\hbar\omega_p \approx 10$ eV, $\lambda_D \approx 2 \times 10^{-8}$ cm, $n_e\lambda_D^3 \approx 1$.

In Eq. (1), Z_T denotes the target ions atomic number, $\overline{Z}$ their ionicity and A_T, the corresponding atomic mass.

The first term on the right hand side (r.h.s) of Eq. (1) extends straightforwardly to electrons bound to partially ionized ions in plasma target, the usual Bethe expression, valid for an isolated ion. This pinpoints an obvious concern about the adaptability of the mean excitation potential I to plasma surroundings. Even more significant is the novel and conspicuous $Z_{eff}(V)$ behavior in a hot plasma target especially at low Z_T. The enhanced projectile ionization in plasma (EPIP) cannot be extrapolated from the usual trends displayed by cold target homologues. It deserves specific developments considered at first, in the sequel.

The stopping expression (1) has been essentially introduced for illustrating a few specific behaviours of projectile ion stopping in a hot plasma medium. Nonetheless, it retains full validity in a high temperature and weakly coupled plasma target as long as the target ions concept remains operationally meaningfull, i.e. as long as its average extension is smaller than the plasma electron screening length λ_D, i.e.

$$\frac{a_0}{Z_T} \leq \frac{743 T_e^{1/2}[\text{eV}]}{n_e^{1/2}[\text{cm}^{-3}]}. \tag{3}$$

When this is not the case, the difference between bound and free target electrons trends become rather blurred. Then, the atomic orbitals are likely to get delocalized around several ions. So, in the weakly coupled regime to which we restrict most of our present attention, the residual and direct ion–ion contribution in the r.h.s of Eq. (1) plays only a minor role (smaller than 5% in most situations of practical interest).

1. Projectile effective charge $Z_{eff}(V_p)$ in a plasma target

We recall the standard Betz expression for the projectile ion effective charge flowing in a neutral and cold gas target, which reads as [4].

$$Z_{eff}(V_p) = Z\left\{1 - 1.034 \times \left[-\left(V_p/2.19 \times 10^8\ [\text{cm/s}]\right)Z^{-0.688}\right]\right\} \tag{4}$$

in terms of the projectile atomic number Z and its instantaneous velocity V_p.

1.1. Hindered recombination

The projectile charge state, in a cold target, gets fixed through a balance between collisional electron losses and bound electron capture of the target atoms. Direct trapping of free electrons is much more problematic to achieve because the excess binding energy has to be evacuated through one of the three processes: (a) radiative recombination, (b) three-body recombination, or (c) dielectronic recombination. Therefore, one should expect different charge states of ions when they pass through plasma or cold targets, except at very high kinetic energy, where bound electron capture is also reduced due to momentum mismatch [5].

In contrast to atomic processes in ordinary plasmas, we emphasize here two specific features: (a) anisotropy of the electron velocity distribution in the ions rest frame, and (b) projectile collisions with target plasma ions are significant.

The dynamical distribution of projectile charge states through target is thus obtained with the coupled equation:

$$\frac{dP_j}{dt} = -P_j\left(\alpha_R^j + \alpha_I^j\right) + P_{j+1}\alpha_R^{j+1} + P_{j-1}\alpha_I^{j-1} \tag{5}$$

where P_j = fraction of projectiles in charge state j, α_R^j, α_I^j = total rate coefficients of recombination and ionization for state charge j.

Given t-dependent outputs rely on charge state, V_p and target parameters. So, the corresponding t-dependent average charge state may be introduced in a standard stopping calculation.

Stopping due to free electrons is derived classically in high temperature plasmas. At each step, energy and velocity data are updated to advance the projectile, up to the following one.

In doing so, temperature effects have been investigated at length (Nardi-Zinamon [6]). Below a 200 eV electron target temperature, ionization of a single electron is the dominant process, mostly for light elements.

Nonetheless, multiple ionization can show up strongly and become the dominant effect especially for heavier projectiles and higher temperatures.

Moreover, kinematic constraints restrict 3-body recombination relative to the radiative one, in particular for highly charged and fast ions. In some cases, a significant dielectronic recombination can outnumber radiative recombination by far.

Finally, the projectile charge state dynamics gets mostly monitored through a balance at equilibrium between collisional ionization and radiative recombination.

At first sight, one seems to recover a statement for coronal equilibrium. However, the restricted electron distribution, in projectile frame, demands that excitation and recombination are performed by same electrons, although with standard Maxwell electrons, excitation arises from the high energy tail of the distribution, while recombination is due to the low velocity part of the bulk.

Typical atomic rates are given on Fig. 1 for ion Cl^{q+} at 1.5 MeV/u.

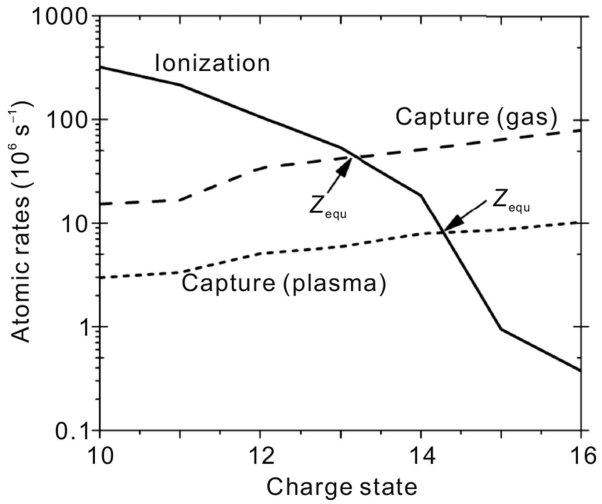

Fig. 1. Ionization and one electron capture rates versus the projectile charge state for Cl^{q+} at 1.5 MeV/u in gas and plasma target. Reproduced from M. Chabot, G. Maynard et al., *Phys. Rev. E* 51, 3504 (1995) with the permission of AIP Publishing.

Outputs of Eq. (5) for ion projectile energy 46 MeV/amu (cf 9 GeV Au ions) are given in Fig. 2(a) (electron-ion excitation) and Fig. 2(b) (ion−ion excitation) for a $Z_T = 10$ ion in target. Such fast ions experience a nearly fully stripped charge state in every situation. Despite that the equilibrium charge is pretty close to the electron-ion case, thus fulfilling Bohr criterion. The time span for the stripping of the first electron is very short, and thus an even decreased initial stripping time does not matter very much. In order to provide a better understanding of the necessary equilibration time, we list in Table 1 the equilibration distance for a constant velocity ion in units of the cold range for the ions in Fig. 2(b).

The delay distances increases swiftly with projectile *Z*. For Au ions, it already amounts to a remarkable one-sixth of the total range.

Fig. 2 demonstrates that impinging projectiles are practically fully stripped at the target entrance. The calculations reported here refer to an electron density $n_e \sim 6 \times 10^{23}$ cm^{-3} i.e. fully ionized aluminum close to solid density.

The stopping rate is roughly proportional to the electron density. Then, once the effective charge state is obtained, it will persist up to near the end of range. Indeed, estimations due to Nardi and Zinamon [6] (Fig. 3) yield a practically constant Z_{eff}, far above cold target counterparts. However, both results converge at highest velocities.

Such an impressive plasma increase of Z_{eff} arises from the hindered free electrons-ion projectile recombination, as compared to the much more favorable one-electron capture from bound electrons which accounts for a three orders of magnitude reduction.

As a result any surviving bound state in target is likely to overwhelm the recombination processes. This picture (Bell [7]) highlights the fact that the target ions with a smaller ionization degree and located close to the projectile trajectory should dominate recombination. Thus, the superposition of

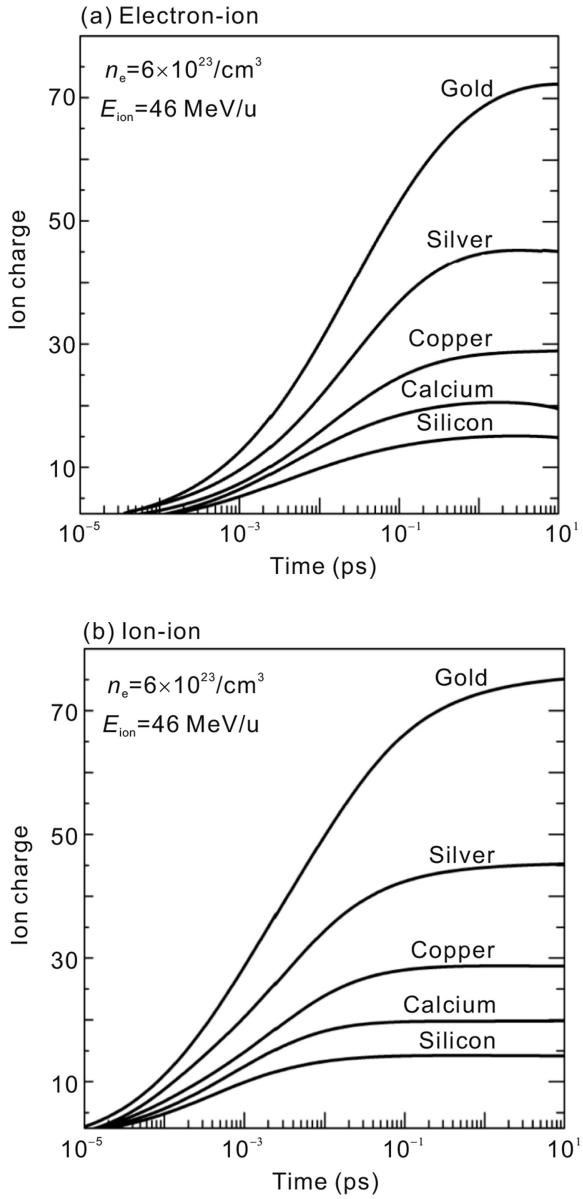

Fig. 2. Time-dependent charge state for several ions with (a) electron collisions and (b) ion collisions for a target corresponding to fully stripped aluminum at solid density. Reproduced from D.S. Bailey, Y.T. Lee and R. More, *J. Phys. (Paris)* C8, 149 (1980) with the permission of EDP Sciences.

Table 1
Equilibration distance (in units of cold range). Calculated with the electron contribution to stripping (Fig. 2(a)) only. When one includes the ion contributions, it reduces substantially.

Ion type	Equilibration distance
Gold	~0.16
Silver	~0.1
Copper	~0.025
Calcium	~0.01
Silicon	~0.005

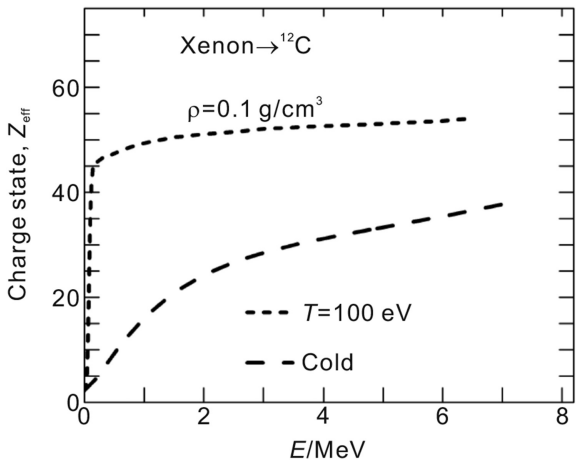

Fig. 3. The charge state $Z_{\rm eff}$ of a Xenon ion as a function of its energy as slowed in a fully ionized Carbon target. Reproduced from E. Nardi and Z. Zinamon, *Phys. Rev. Lett*. 49, 1251 (1982) with the permission of AIP Publishing.

accurate stopping estimates with a specific $Z_{\rm eff}(V_{\rm p})$ in plasmas produces an enhanced range shortening.

1.2. Basic mechanisms

Total rates $\alpha_{\rm R}^j$ and $\alpha_{\rm I}^j$ appearing in Eq. (5) refer to sums over individual loss and capture rate processes $\sum_i \alpha_i$ with [8]

$$\alpha_i(V_{\rm p}) = \int {\rm d}\boldsymbol{V} f_i(\boldsymbol{V},\boldsymbol{V}_{\rm p})\sigma_i(|\boldsymbol{V}_{\rm p}|)V \tag{6}$$

taken in a projectile moving frame, in terms of a shifted Maxwell distribution f_i for the plasma particles (mass m, number density n and temperature T) with thermal velocity V,

$$f_i(\boldsymbol{V},\boldsymbol{V}_{\rm p}) = n_i\left(\frac{m}{2\pi k_{\rm B}T}\right)^{3/2} {\rm e}^{-\frac{m}{2\pi k_{\rm B}T}\left(V-V_{\rm p}\right)^2} \tag{7}$$

and adequate cross-sections $\sigma_i(|\boldsymbol{V}_{\rm p}|)$ for the projectile-plasma particles interaction. n and T designate plasma density and temperature, respectively.

The actual efficiency of a computer code calculation relies heavily on the approximate expressions used for $\sigma_i(|\boldsymbol{V}_{\rm p}|)$. We detail below a few amongst the most significant. To keep presentation at a decent complexity level, one restricts first to a simple Slater model for the screened and hydrogenlike basic atomic quantities, such as excitation energies and oscillator strengths in plasma target. Nonetheless, the essential $\sigma_i(|\boldsymbol{V}_{\rm p}|)$ behaviors featuring ionization and recombination are still given a proper perspective.

1.2.1. Ionization by plasma particles

First, we consider the one-electron excitation of projectile ions colliding with target free electrons and ions (denoted by A) respectively:

$$X^{q+} + {\rm e} \to X^{q+*} + {\rm e}',$$
$$X^{q+} + A^{p+}(E) \to X^{q+*} + A^{p+}(E').$$

The above two processes are only significant for a deexcitation time which is long compared to intercollision time. Similarly, ionization through collisions with target free electrons and ions is given as:

$$X^{q+} + {\rm e} \to X^{(q+1)+} + 2{\rm e},$$
$$X^{q+} + A_j^{p+} \to X^{(q+1)+} + A_j^{(p-1)+},$$
$$X^{q+} + A_j^{p+} \to X^{(q+1)+} + A_j^{p+} + {\rm e}.$$

They feature the most important contribution to projectile ionization. $\alpha_{\rm ie}$ refers to the electron reaction rate averaged over electron distribution and $\alpha_{\rm ij}$ denotes a similar quantity for the sum of the following ion processes (see Eq. (6)). Autoionization matters when the projectile ion is doubly excited, with one electron ionized and the other one deexciting into a lower level.

One of the simplest and more robust modeling of projectile ionization by electrons and ions in the target is the well-known binary encounter model (BEM) introduced in a classical framework by Gryzinski [9]. According to this model, the cross-section for removing an electron in the n shell projectile ion cloud, by target ion impact is given as:

$$\sigma_{\rm BEM} = \sum_n N_n\sigma_n = \sum_n N_n\pi\left(\frac{Z_{\rm T}e^2}{U_n}\right)^2 G\left(\frac{V_{\rm p}}{V_n}\right). \tag{8}$$

Here, N_n is the number of electrons in the nth shell, U_n is their binding energy, and $V_n = \sqrt{2U_n/m}$ their orbital velocity.

G is derived through the matching $V_{\rm p} \simeq V_n$ for optimal ionization. It reads as:

$$G(V) = \frac{\alpha^{3/2}}{V^2}\times$$

$$\left\{\alpha + \frac{2}{3}(1+\beta)\ln(2.7+V)\times(1-\beta)\left[1-\beta^{\left(1+V^2\right)}\right]\right\}, \tag{9}$$

$$\text{for } V > 0.206,$$

$$G(V) = 4V^4/15, \quad \text{for } V < 0.206,$$

where $\alpha = V^2/(1+V^2)$, $\beta = 1/[4V(1+V)]$.

According to its velocity $V_{\rm p}$, the ion projectile is penetrating more or less deeply into a target atom or ion. Following Bell [7], one can approximate $\overline{Z}$ as the charge within a sphere of radius $b_n = \sqrt{\sigma_n/\pi}$.

$\alpha_{\rm BEM} = V_{\rm p} n \sigma_{\rm BEM}$ denotes Coulomb ionization rate. The upper dashed line in Fig. 4 shows the rate coefficient for the case of an iodine beam with $V_{\rm p} = 1.5\alpha c$ and $\alpha = \frac{1}{137.036}$, fine structure constant in a hydrogen plasma with temperature $T = 10$ eV and ion density $n_{\rm i} = 10^{17}$ cm^{-3}. The relative fraction of bound electrons in such a plasma is no larger than 2×10^{-6}.

The ionization edge (lower dashed curve in Fig. 4) documents a significant difference between ionization processes arising from target ions or target electrons.

Electrons such as $V_{\rm r} < V_n$ do not have enough kinetic energy to ionize an nth shell bound electron. So, according to Lotz [10], ionization through free electron collisions features the cross section:

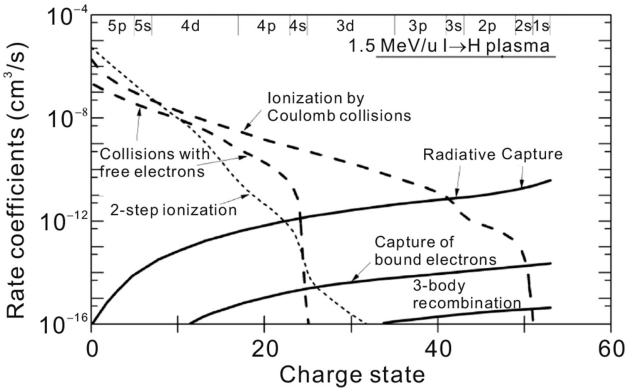

Fig. 4. Rates of electron capture and loss for a 1.5 MeV/u iodine beam in a 10 eV hydrogen plasma with $n_e = 10^{17}$ cm^{-3}. The intersection between capture and loss is close to the equilibrium charge $Z_{eq}(V_p)$ at constant velocity (arrow). Atomic shells corresponding to charge states are given at the top. Reproduced from Th. Peter and J. Meyer-Ter-Vehn, *Phys. Rev.* A 43, 2015 (1992) with the permission of AIP Publishing.

$$\sigma_e = \sum_n N_n \sigma_n = 4\times 10^{-14}\left[(\mathrm{cm}\cdot\mathrm{eV})^2\right] \times \sum_n \frac{\ln\left(\frac{E_r}{U_n}\right)}{E_r U_n}\theta(E_r - U_n) \tag{10}$$

with the step function $\theta(x) = (|x| + x)/2$.

The relative energy between plasma electron and projectile ion is approximated by $E_r = (m/2)V_r^2 \simeq (m/2)(V_p^2 + V_{the}^2)$, where V_{the} is the thermal velocity of plasma electrons. The rate is $\alpha_e \simeq V_r n_e \sigma_e$. The edge at I^{24+} to I^{25+} in Fig. 4 pertains to the transition from the N shell to the M shell; the electrons do not have enough energy for M-shell ionization.

1.2.2. Radiative electron capture and three-body recombination

Radiative recombination:

$$X^{q+} + e \rightarrow X^{(q-1)+} + h\nu$$

has to be taken into account for highly ionized targets, and α_{REC} is the corresponding reaction rate averaged over free-electron distribution.

Radiative electron capture (REC) is explained by the electronic transition probability $A(n' \rightarrow n)$ between major shells $n' \rightarrow n$ for the projectile (charge state Z) with energy $E'_n - E_n = \hbar\omega$. In the quasiclassical approximation (Zel'dovich and Raizer [11]),

$$A(n' \rightarrow n) \propto \left[\frac{Z^2}{n^2} - \frac{Z^2}{n'^2}\right]^2 \left|\frac{1}{n^3} \times \frac{1}{n'^3}\right| \frac{1}{\left(\frac{1}{n^2} - \frac{1}{n'^2}\right)}. \tag{11}$$

The free-bound transition in the REC process can be derived from Eq. (11) through $n' \equiv i\kappa$, where κ is the inverse velocity v of the photoelectron in αc units.

$$\begin{aligned} A(n' \rightarrow n)\mathrm{d}\kappa &\propto \frac{Z^4}{n^3}\frac{1}{\left(\frac{1}{n^2} + \frac{1}{\kappa^2}\right)}\frac{\mathrm{d}\kappa}{k^3} \\ &\propto \frac{Z^4}{n^3}\frac{1}{\left(\frac{1}{n^2} + V^2\right)} V\mathrm{d}V. \end{aligned} \tag{12}$$

A $\mathrm{d}\kappa$ is proportional to the rate of REC into the nth projectile shell $(\sigma_n v)\mathrm{d}^3 v = (\sigma_n v)4\pi v^2 \mathrm{d}v$.

One thus gets [12]:

$$\sigma_n = A\frac{V_0}{V}\frac{h\nu_0}{\frac{m_e}{2}V_r^2}\frac{g}{n^3} \tag{13}$$

where:

$$A = 2.1\times 10^{-22}\frac{2^4}{3^{3/2}}\frac{he^2}{m_e^2 c^3}\ \left[\mathrm{cm}^2\right],$$

$$h\nu = \frac{1}{2}m_e V_r^2 = \frac{h\nu_0}{n^2},\ h\nu_0 = Z^2\ [\mathrm{Ry}],$$

g is the free-bound Gaunt factor, $g \approx 1$.

The total rate $\sigma_{REC} = V_r n_e \sigma_{REC}$ is then determined by a sum from the ground state n_g (N_{n_g} electrons) up to large quantum numbers. In the hydrogenlike approximation

$$\alpha_{REC} = \left(1 - \frac{N_{n_g}}{2n_g^2}\right)\alpha_{n_g} + \sum_{n=n_g+1}^{\infty}\alpha_n. \tag{14}$$

The quantity α_{REC} shows up in Fig. 4 as a solid line.

At high density the probability for a simultaneous collision of the projectile ion with two electrons increases. One of these electrons is then captured by the projectile, while the other carries away the excess energy. The 3-body process thus reads as

$$\begin{aligned} \alpha_{3BR} &= \frac{2^5\pi^2 e^{10}}{m^5}\frac{Z^3 n_e}{V_r^9} \\ &= 2.92\times 10^{-31} Z^3 \frac{n_e}{V_r}\left[\frac{\mathrm{cm}^3}{\mathrm{s}}\right], \end{aligned} \tag{15}$$

contrasted to radiative electron capture (V_r in αc, n_e in cm^{-3}):

$$\frac{\alpha_{REC}}{\alpha_{3BR}} \approx 1.6\times 10^{17}\frac{\frac{Z^4}{V_r^3}g n_e}{\frac{Z^3 n_e}{V_r^9}n_e} = 1.6\times 10^{17}\frac{ZV_r^6}{n_e}. \tag{16}$$

Regarding to laboratory plasmas, radiative electron capture remains many orders of magnitude larger than three-body recombination. For 1.5 MeV/u ion projectiles ($V_r = 7.75\ \alpha c$) the two rates are equivalent when the density is close to solid-state one (Fig. 5).

1.2.3. Capture of bound target electrons

In partially ionized targets, a bound electron can jump from a target ion to the projectile (charge transfer (CT)). Oppenheimer and Brinckmann and Kramers [13] evaluated the cross section (OBK theory) for this process in first Born approximation for the Coulomb potential $-e^2/r$ and hydrogenlike wave functions (Laguerre polynomials). Using the cross section averaged over all initial (l, m) states and summing over all final (l, m) states,

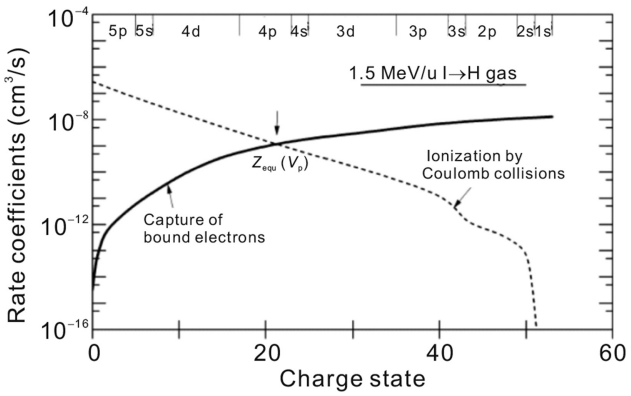

Fig. 5. Rates for 1.5 MeV/u iodine in cold hydrogen gas with $n_e = 10^{17}$ cm^{-3}. Here the equilibrium charge is about 21 (arrow), thus considerably less than in the plasma case (Fig. 4). Reproduced from Th. Peter and J. Meyer-Ter-Vehn, *Phys. Rev.* A 43, 2015 (1992) with the permission of AIP Publishing.

$$\sigma_{CT} = 4.1 \times 10^4 \sum_{n_i} \sum_{n_f} N_i a_{eik} \times \frac{\left(Ze^2\right)^2 E_i^{5/2} E_f^{3/2} E_k^4}{\left[E_k^2 + 2E_k\left(E_i + E_f\right) + \left(E_i - E_f\right)^2\right]^5} \tag{17}$$

where E_i and E_f are the binding energies of the electron >0 in initial and final states, respectively, Z is the charge state of the projectile $E_k = mV_p^2/2$, and N_i the number of electrons in the shell of the target. a_{eik} features a reduction factor (in the usual OBK theory $a_{eik} = 1$). Generally $0.1 \lesssim a_{eik} \lesssim 0.4$.

Fig. 4 adds to all the other processes also the charge-transfer-rate coefficient in the 10-eV plasma that stems from the small part (2×10^{-6}) of bound electrons. For comparison Fig. 5 also exhibits rate coefficients in a cold hydrogen gas of the same density 10^{17} cm^{-3}. The total loss rate in both cases does not differ much from each other, but capture drops in the plasma case by about three orders of magnitude.

At large projectile velocities, one gets

$$\frac{\alpha_{CT}}{\alpha_{REC}} \approx 10^9 \frac{Z^2 E_i^{5/2} \frac{E_f^{3/2}}{V_p^{11}}}{\frac{Z^4}{V_p^3 n_f^3}} \cong 10^9 \frac{E_i^{5/2} Z}{V_p^8 Z_T} \tag{18}$$

with E_i in Ry and V_p in αc. In cold plasmas with many bound electrons OBK rate ranks many orders of magnitude above radiative recombination.

1.3. Master equation

It looks now appropriate to systematize the overall effect of every basic mechanism on the inflight ion projectile charge state. During its penetration into a target, this charge state continuously fluctuates through gain and loss of electrons. It appears then convenient to focus attention towards the population P_n of a given excited state n of the ion projectile. Recalling that on a spherical electron shell n, there are $2n$ available locations, one can establish at once a masterlike relationship for the P_n evolution in terms of loss and gain reaction rates as [14].

$$\frac{dP_n}{dt} = -P_n \left[l(n,n) + \sum_{k \neq n} \left(2k^2 - P_k\right) l(n,k) \right] + \left(2n^2 - P_n\right) \left[g(n,n) + \sum_{k \neq n} P_k g(k,n) \right], \tag{19}$$

which obviously extends Eq. (5) to arbitrary excited state n with every former basic mechanism included, dielectric recombination excluded.

When $k \neq n$, $l(n, k) = g(n, k)$ represents the rate coefficient for one electron transfer from level n to level k, provided there is one electron in level n and one free place available in level k; $g(n,n)$ and $l(n,n)$ denote rate coefficients for recombination and ionization, respectively. l and g are computed owing to electron and ion ionization and excitation, spontaneous decay, bound–bound and radiative recombination. Eq. (19) has to be changed somewhat to include dielectronic recombination and autoionization process.

1.4. Dielectric recombination

In view of its rather involved behaviour, we postponed up to here a thorough presentation of the dielectric recombination (DR) effect on the projectile charge state evolution.

1.4.1. Basic mechanism

Dielectronic recombination:

$$X^{q+} + e \rightarrow \left(X^{(q-1)+}\right)^{**} \rightarrow X^{(q-1)+} + h\nu$$

is a two-step process in which a free electron with kinetic energy E_k is captured by an ion X of charge Z and the excess energy is transferred to another electron already bound in shell $i \equiv (n_i l_i)$, which will be excited to shell $j \equiv (n_j l_j)$. This writes as

$$X(Z,i) + e(E_k, l \pm 1) \xrightarrow{A_a} X^{**}(Z-1, jnl). \tag{20}$$

The free electron will be captured into a highly excited level $n \gg 1$, from where it will get autoionized by process Eq. (20) running from right to left (Auger effect with rate A_a). X^{**} is then deexcited via a stabilizing radiative decay (with rate A_r) i.e.

$$X^{**}(Z-1, jnl) \xrightarrow{A_r} X^{*}(Z-1, inl) + \hbar\omega \tag{21}$$

The photon carries the energy $\hbar\omega = E_j - E_i$ out. With its longer lifetime the higher excited electron remains after the $i \rightarrow j$ transition in the (n, l) level, and it finally cascades down to ground state. Here only the decay to state i is considered [8].

The basic DR features which includes resonance condition and fluorescence yield are pictured on Table 2.

Energy conservation demands $E_k - E_{nl} = E_j - E_i$, where E_k is the kinetic energy of the free electron, E_i the binding energy

of the initially bound electron (possibly in an inner shell), and E_j and E_{nl} the energies of the excited states. We restrict to an ion at rest in target plasma. The number of DR processes per unit volume and time is $n(X^{**})A_r/n(X)n_e$.

Detailed balance to the total loss of doubly excited ions $n(X^{**})(A_a + A_r)$ is given by the loss $n_{Saha}(X^{**})A_a$ in a Saha equilibrium

$$n(X^{**}) = \frac{A_a}{A_r + A_a} n_{Saha}(X^{**}), \tag{22}$$

where n_{Saha} is given by

$$\frac{n_{Saha}(X^{**})}{n(X)n_e} = \frac{g(Z-1, jnl\pm1)}{2g(Z,i)} \frac{h^3}{(2\pi m k_B T)^{3/2}} e^{-E_k/k_B T}. \tag{23}$$

Here, $g(Z,i)$ and $g(Z-1, jnl\pm1)$ are statistical weights of the states $X(Z,i)$ and $X^{**}(Z-1, jnl\pm1)$, so that

$$\begin{aligned} &g(Z,i) \equiv \binom{g_i}{N_i}\binom{g_j}{N_j},\ g(Z,j) \equiv \binom{g_i}{N_i+1}\binom{g_j}{N_j+1}, \\ &g(Z-1,jnl) \equiv \binom{g_i}{N_i-1}\binom{g_j}{N_j+1} 2(2l+1) \end{aligned} \tag{24}$$

where

Table 2
The dielectronic recombination mechanism.

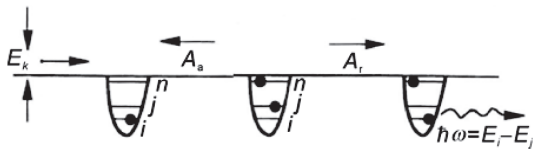

STEP①: Radiationless Capture "→"
(autoionization "←")
$X(Z, i)$+e(E_k,1) → $X^{**}(Z\text{-}1; j, n\ell \pm 1)$

STEP②: Stabilizing Radiative Transition
$X^{**}(Z\text{-}1; j, n\ell \pm 1)$ → $X^{*}(Z\text{-}1; i, n\ell \pm 1)+\hbar\omega$

(a)

$$E_k + E_n = E_i - E_j$$
$$E_k + \left(\frac{Z}{n}\right)^2 = \left(\frac{Z+1}{i}\right)^2 - \left(\frac{Z+1}{j}\right)^2$$

Energy matching condition

"Branching Ratio"

$$\left(\frac{dX^{**}}{dt}\right)_r = -A_r X^{**}\ ,\quad \left(\frac{dX^{**}}{dt}\right)_a = -A_a X^{**}$$

(b) $\alpha_{DR} \propto A_a \frac{A_r}{A_a + A_r}$

$g_i = 2(2l_i),\ g_j = 2(2l_j + 1)$.

N_i and N_j are occupation numbers of shells in i and j of the ion $X(Z, i)$. Hence the DR rate specified by the quantum numbers (i, j, nl) appears as:

$$\begin{aligned} &\alpha_{DR}(i,j,nl) \\ &= \frac{A_r(j\to j)A_a(jnl\to iE_k l\pm1)}{A_r(j\to j) + A_a(jnl\to iE_k l\pm1)} \\ &\times \frac{g(Z-1, jnl\pm1)}{2g(Z,i)} \\ &\times \frac{h^3 n_e}{(2\pi m k_B T)^{3/2}} e^{-(E_j - E_i + E_{nl})/k_B T}\ , \end{aligned} \tag{25}$$

with $A_r A_a/(A_r + A_a)$, branching ratio or fluorescence yield.

The total rate of DR [15].

$$\alpha_{DR} = \sum_{i,j,nl} \alpha_{DR}(i,j,nl) \tag{26}$$

consists of a large sum over electronic states where (n, l) denotes the states into which the plasma electron is captured with a simultaneous excitation of a projectile electron from state i to state j. $E_k = mv^2/2$ is the initial kinetic energy of the recombining electron in the rest frame of the projectile. In the beam-plasma case, the projectile sees a Maxwellian electron distribution (6) shifted by the projectile velocity V_p. The corresponding rate

$$\alpha_{DR}(V_p) = \int d^3v f(v, V_p) v \sigma_{DR}(v), \tag{27}$$

is easily obtained from the normal plasma rate $\alpha_{DR}(V_p = 0)$ if we take into account that the cross section $\alpha_{DR}(V_p = 0)$ from the work of Jacobs et al. [16]. Then one obtains

$$\alpha_{DR}(V_p) = \left(\frac{4\pi a_B^2 E_H}{k_B T}\right)^{3/2} \sum_{i,j,nl} \frac{g(j,nl)}{2g(i)} \times \frac{A_a A_r}{A_a + A_r + A_a^v} F(s,t), \tag{28}$$

with $a_B = \hbar^2/me^2$ and $E_H = e^2/2a_B$; $g(j,nl)$ and $g(i)$ are statistical weights. The l dependence of the Gaunt factor g_l in A_a is normalized to $\sum g_l = 0.2$. As a novel feature, autoionization of valence electrons (rate A_a^v) in addition to autoionization of the captured electron (rate A_a) is found to be important in certain open-shell ions and has been included in Eq. (28).

The function

$$F(s,t) = \left\{\exp\left[-(s-t)^2\right] - \exp\left[-(s+t)^2\right]\right\}/4st \tag{29}$$

in Eq. (28) results from the integral (27) with

$$s^2 = \frac{E_j - E_i + E_{nl}}{k_B T} \quad \text{and} \quad t^2 = \frac{mV_p^2}{2k_B T}.$$

In the limit $V_p = 0$, the pure plasma result with the Boltzmann factor $F = \exp[-(E_j - E_i + E_{nl})k_B T]$ is recovered

from Eq. (28) and the rate is largest for high temperatures with $E_j - E_i \cong \frac{3}{2}k_B T$. However, for fast ions in plasma of low temperature ($V_p \gg V_{th}$), the resonance condition is best fulfilled for

$$\frac{mV_p^2}{2} \cong E_j - E_i + E_{nl} \gg k_B T (s \cong t \gg 1),$$

the beam then probes individual resonance states as a function of beam velocity with a width $k_B T$.

1.4.2. Balance equation

In order to include dielectronic recombination (DR), and the inverse autoionization process (AP) in the master expression (19), we reconsider [17].

$$e + A(P_i, P_j, P_k) \underset{2}{\overset{1}{\rightleftarrows}} A(P_{i-1}, P_{j+1}, P_{k+1}) \tag{30}$$

where $A(P_i, P_j, P_k)$ refers to a projectile with P_i, P_j, P_k electrons in levels i, j and k respectively (k, $j > i$). Reaction 1 pertains to DR and 2 to AP. In view of expression (19) one has for the rates τ_1 and τ_2:

$$\tau_1 = P_i(2j^2 - P_j)(2k^2 - P_k) d(i,j,k) \tag{31}$$

and

$$\tau_2 = P_j P_k (2i^2 - P_i) a(i,j,k) \tag{32}$$

with $d(i, j, k)$ and $a(i, j, k)$ the rate coefficients for one electron or one free place in each level. τ_2 implies that P_j and P_k behave as independent quantities, which is roughly true in a high density plasma where numerous collisions can occur, but not in the low density case where the deexcitation time is now smaller than the collision time. In that case the approximation of independent populations leads to a very low and unphysical τ_2 as already mentioned in Ref. [18].

Adapting the DR expressions given in Section 1.5.1, to the present formulation we explain τ_1 through

$$d(i,j,k) = \frac{15.28 \times 10^{16} E_k \omega F_{ij} F(\sqrt{\omega})}{2k^2 2j^2 k (\Delta E)^2 \lg\left(2k\sqrt{\frac{\Delta E}{E_k}}\right)} \sum_{l=0}^{k-1} \frac{1}{2l+1} \tag{33}$$

with $\Delta E = E_j - E_i$ (Ry), F_{ij} is the dipole oscillator strength, $\omega = E_k + E_j - E_i$ (Ry) and l the azimuthal quantum number of level k. The function F is given by

$$F(g) = T \frac{\left\{\lg\left[1 + \exp\left(\alpha - \frac{g+V_p^2}{T}\right)\right] - \lg\left[1 + \exp\left(\alpha - \frac{g-V_p^2}{T}\right)\right]\right\}}{4gV_p}$$

with T denoting the temperature (Ry) and α the degeneracy of plasma free electrons (V_p in a.u.).

τ_2 is derived from micro-reversibility with the l dependence carefully included. When we use micro-reversibility we can start either from $d(i,j,k)$ and calculate $a(i,j,k)$, or start from $d^l(i,j,k)$ at a given quantum number l which leads to $a^l(i,j,k)$ and then sum over the number of electrons with quantum number l in level k, noted $P(k,l)$, to finally reach $a(i,j,k)$. The two calculations yield the same result only for a random distribution $P(k,l) = P_k[(2l+1)/2k^2]$. In that case one gets

$$a(i,j,k) = \frac{3.819 \times 10^{16} E_k \omega F_{ij}}{2j^2 k (\Delta E)^2 \lg\left(2k\sqrt{\frac{\Delta E}{E_k}}\right)} \sum_{l=0}^{k-1} \frac{1}{2l+1}. \tag{34}$$

But if we consider a low density plasma with a collision time much longer than the deexcitation time, then one has to put $P(k,l) = P_k$ and the rate coefficient gets multiplied by $(1/\theta)$ with

$$\theta = \sum_{l=0}^{k-1} \frac{1}{2l+1} \Bigg/ \left[k^2 \sum_{l=0}^{k-1} \frac{1}{(2l+1)^2}\right]$$

We thus make the approximation to use Eq. (34) for a random population of electrons that do not come from DR whereas the coefficient a/θ provides the AP rate for electrons that result only from DR.

It must be emphasized here that DR and AP are two independent processes. In a high density plasma AP is the dominant effect because the excited states are populated mostly by collisions. In this case the overall effect of DR and AP is a loss of electrons.

1.5. Balance steady state

The above detailed atomic processes can suitably be given a perspective with the study of realistic ion-plasma interactions.

1.5.1. General

Projectile ionization stages get constantly modified through ion-electron and ion–ion collisions in the target. Most significant ones include collisions with free plasma particles, while autoionization also affects the projectile effective charge. Other mechanisms of noteworthy to be mentioned also include bound–bound charge transfer from plasma bound electrons, radiative transfer, while non 2-body recombinations (dielectronic and 3-body) provide only negligible contribution even at high densities and are not considered any further. Internal projectile charge state is also submitted to excitations caused by target particles and also to spontaneous projectiles radiative decay. Low density targets feature projectiles mostly in the ground state, which restricts considerations to total cross-sections.

This point of view is illustrated on Fig. 6 with atomic collision rates for 4 MeV/u I^{q+} ions in helium plasma with $n = 4 \times 10^{17}$ cm^{-3} and $T = 4.4$ eV. These parameters give rise to a plasma ionization degree $z = 0.5$.

From Figs. 1 and 6 the equilibrium charge state Z_{eq} is obtained when ionization rate matches the recombination one. Ionization rates arise through ion collisions (Fig. 6) while recombination rate arises from charge transfer yielding $Z_{eq} = 31$. Looking now at the rate τ_{eq} for this $q = Z_{eq}$ we can have an estimate of the necessary time for the ion to reach its

equilibrium charge, keeping its velocity constant, by defining the equilibrium time $t_{eq} = 1/\tau_{eq}$.

Atomic rates (Fig. 6) are given as frequencies for projectiles gains and losses of electrons, thus establishing a rate for a relative charge variation 1/q. In the same vein, one gets a stopping rate R_{stp} for a relative energy variation of $\Delta E/E = 1/q$ and $R_{stp} = qSV/E$ which is also reported in Fig. 6 in terms of the stopping power $S = -\mathrm{d}E/\mathrm{d}x$.

Aside from density dependence, every mechanism involved in the evolution of the ion projectile charge while crossing in plasma is given on Fig. 6.

As an example, we now consider an iodine ion with a given ionization state q. For instance, let us take an initial value $q = 24$. Fig. 6 tells us that this ion should be ionized by collisions with plasma ions until reaching $Z_{eq} = 31$ with a time $t_{eq} = 5$ ns.

Then, the atomic rate is 10 times above the stopping rate, and the q increases from 24 up to 31 preventing the projectile from slowing down, since the target length required from reaching equilibrium amounts to 13.8 at the given density.

Removing charge transfer, the projectile ion charge increases up to $q = 38$ through ion collisions when ionization rate balances the stopping rate. The given ionization stage defines the dynamical charge Z_{dy}.

Energy changes more swiftly than the charge state during the slowing down process, when $q \geq Z_{dy}$. Then, the projectile charge stays unchanged until energy decays sufficiently with a recombination rate $>R_{stp}$.

These considerations thus allow us to foresee from Fig. 6 the evolution of the projectile charge state in terms of target parameters through the behaviour of most significant atomic rates.

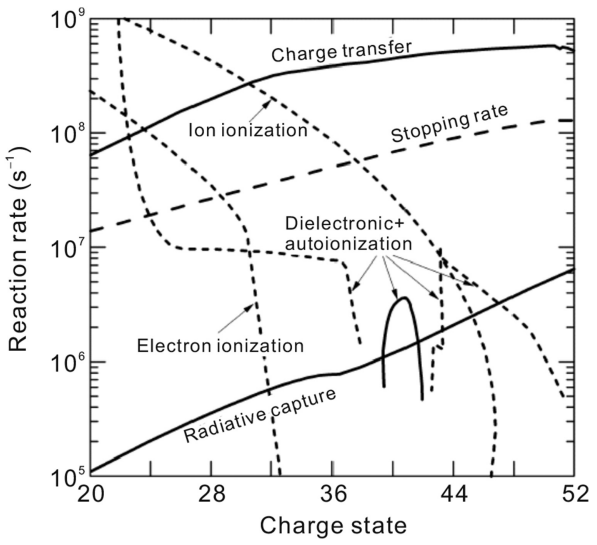

Fig. 6. Reaction rates for electron capture (solid line) and loss (dashed lines) together with stopping rate (dotted curve) of 4 MeV/u I^{q+} in half-ionized helium plasma at $T = 4.4$ eV and $n = 4 \times 10^{17}$ cm^{-3} as a function of projectile charge state q. [G. Maynard et al., *Nuo. Cim.* 106 A, 1825 (1993)] with kind permission of Societa Italiana di Fisica, copyright 2016.

Overall low-density plasma trends then feature:

1. All of the rates are almost directly proportional to the density.
2. Electron collision ionizations do not play a significant role.
3. Free electron capture can only appear for highly collisional plasma.
4. Ion-ion collision rates nearly scale as Z^2 for not too high atomic number. The stopping rates experience little variations with density due to plasmon energy in the Bethe formula. Ion-ion collisions are insensitive to plasma ionization.
5. Charge transfer decreases with plasma ionization so does the total recombination rate.

At first sight, modifying $\overline{Z}/Z_T$ has not much bearing on curve slopes. A trend can be predicted by moving up or down (in Fig. 6) the three curves of ion collision ionization rate, stopping rate and bound-bound charge transfer rate. The plasma atomic number has a large influence on ionization and charge transfer probability, while plasma ionization modifies the stopping rate and charge transfer. In an energetic ion-plasma encounter ion-ion collisions are more relevant than the electron-ion ones, at variance with collisions between plasma particles, which rules out collisional radiative models in the present situation.

1.5.2. Temperature effects

An obvious temperature signature stems from the quadrature of electron-ion collisions cross-section over the plasma electron velocity distribution in the moving projectile frame. As in the stopping expression, temperature leaves an immediate imprint for $V_p \leq V_{the}$. However, electron ionization stays below ion ionization and free electron recombination remains under the stopping rate. So, the temperature does not directly influence the projectile charge dynamics. Nonetheless, charge transfer relies on plasma excitation and ionization $\overline{Z}/Z_T$. Ion-ion ionization hardly changes with increasing $\overline{Z}/Z_T$, the main effect of which is to lower the charge transfer rate, yielding (Fig. 6) enhanced Z_{eq} and bigger t_{eq}. Z_{eq} is only obtained at a large enough plasma linear density. When $\overline{Z}/Z_T$ keeps rising up, charge transfer rate falls below the stopping rate and the projectile charge now relies on initial q value. When $q < Z_{dy}$, the projectile charge attains $q = Z_{dy}$ with decreasing energy, while if $q > Z_{dy}$ energy decays even faster with nearly unmodified projectile charge state. $\overline{Z}$ induced recombination arises from enhanced bound-bound charge transfer monitored by the strongly bound electrons. In hydrogen target, recombination is usually proportional to bound electron density while a large ionization will allow dielectronic and radiation processes to occur. In other targets, significant reduction of recombination only occurs for K and L ionized electrons and also at a large temperature. The influence on the enhanced projectile ionization in plasma (EPIP) reaches its top value in fully ionized targets with a small Z_T and shows us as negligible at a high Z_T [20].

1.5.3. Dynamical effect

As seen previously, a dynamical imprint appears for R_{stp} bigger than any atomic state. Fig. 6 demonstrates it appearing at reduced recombination with $q \geq Z_{dy}$. At not too big Z_T, the ionization rate is proportional to Z_T and the charge transfer rises even swifter with Z_T, with a nearly Z_T-independent stopping rate. Dynamical effect is then triggered by small atomic numbers. In heavy targets, the projectile charge remains close to Z_{eq}. Cold hydrogen targets document nonequilibrium charges while strong dynamical effects demand full target ionization. Moreover, in a fully ionized He target, a 4 MeV/u iodine beam with an initial charge below $Z_{dy} = 58$, will rapidly attain it. As ion projectile slows down, ionization turns smaller than stopping.

As a result, ionization remains constant until the radiative or dielectronic recombination rate is above the stopping rate, at a very low projectile velocity.

In a mundane situation featuring large target ionization and an initial ion projectile charge state $<Z_{eq}$, the projectile will be keeping a nearly constant charge $\sim Z_{dy}$ on most of its trajectory for $E = E(0)$, the initial energy.

The slowing down process is initiated with a charge $<Z_{eq}$ while it turns $>Z_{eq}$ further on. This fixed charge process largely influences the energy deposition profile. Although nearly flat, in cold targets, the swift heavy-ion energy profile becomes proton-like, featuring a Bragg peak near the end of range as it is the case in strongly ionized plasmas targets. In the latter case, stopping slightly decreases with density (plasmon energy in Bethe expression) so that solid targets exhibit less dynamical effects than plasma ones.

Dielectronic and autoionization (DA) processes account for electron losses except for a resonance at $q \sim 38$. DA documents autoionization after a dielectronic recombination and also arises from vacancies out of plasma ion collisions. Autoionization rate $\sim z^2$ (z denoting degree) can rank high in large Z_p targets.

1.5.4. Density effects

Density highlights a rather tricky case featuring pretty large uncertainties due to the use of partial cross-sections. We shall mainly focus on the density impact on ion projectile excitation. Every atomic rate is proportional to target density at the exclusion of radiative decay and autoionization. In the presence of an increasing density, the incoming ion has no time to relax to ground state between two collisions in a row. Then, a few collisions later, it can pile up enough excitation energy available for Auger emission at surface exit. The main density effects are: excitation collision effect, partial recombination effect and vacancy production effect. Obviously, excitation arises because excited states are easier to ionize than ground state. With the excitation cross-section $\sim Z_p^2$ such an effect appears first in a heavy material. Excitation collisions are documented by the Betz–Grodzins model [19] for a projectile endowed with a number of weakly excited electrons [19]. A small enhancement will secure ionization with a large Auger emission taking place at surface exit.

Recombining electrons on high lying levels may trigger ionization in lieu of transfer. Partial recombination on excited levels rises with decreasing z. The recombination reduction via partial charge transfer remains small for heavy targets and features a dominant density effect at low Z_p. For instance, in a hydrogen target with $n = 10^{20}$ cm^{-3}, the given diminution rises Z_{eq} from 24 to 29 for a 1 MeV/u iodine beam. Low Z_p targets favor the Bohr-Lindhard model highlighting a large density enhancement for the projectile in plasma and some Auger electrons at target exit.

On the other hand, low Z_p targets stress a density dependence through vacancies in ion projectile inner shell. Then, electrons are allowed to recombine on high-lying levels but are not allowed to do so in a vacancies produced by ion collisions. The charge then increases with density in relation to excitation rates higher than radiative decay rates and also the vacancies number increases with density. This effect seems to be the largest for carbon targets.

Finally, it should be noted that systematic discrepancy between q exit and q outside prevents a straightforward experimental vindication of density effect on heavy ion charge state within target. Nonetheless, recent stopping power measured data demonstrate a 15% increase for the heavy ion effective charge in solid when contrasted to the equivalent cold gas.

1.6. Inflight effective charge (hydrogen target)

Now we can integrate all those atomic rates into a complete calculation of the ion projectile velocity-dependent effective charge $Z_{eff}(V_p)$. We focus attention on I^{N+} in view of its high resonant contribution to dielectronic recombination. So, it can provide a convincing benchmark for optimizing the impact of this effect on inflight projectile charge state.

1.6.1. Solution of the rate equation neglecting dielectronic recombination

The total rates for ionization and recombination without dielectronic recombination thus read as:

$$\begin{aligned} \alpha(Z \rightarrow Z+1) &= \sigma_{BEM}(Z) V_p n_i + \sigma_e(Z) V_r n_e \\ \alpha(Z \rightarrow Z-1) &= \sigma_{CT}(Z) V_p n_i + \sigma_{REC} + \sigma_{3BR}(Z) V_r n_e \ , \end{aligned} \tag{35}$$

which allow to solve the rate equations for 1.5 MeV/u iodine ions incident on 10 eV hydrogen with a density of 10^{17} cm^{-3}. Fig. 7, displays the charge-state evolution starting from $Z_{eff} = 0$. For $V_p = 10\alpha c$ we find $E_{eq,hot} \gg E_{eq,cold}$. Only at very high velocities is $Z_{eq,hot} \leq Z_{eq,cold}$ because according to Eq. (18), the cross section for charge transfer drops faster at high velocity than the cross section for high radiative capture.

Fig. 7 also reveals that the equilibrium areal density $\int n_e dl$ (integrated from $Z = 0$ to $Z = Z_{eq} - 1$) increases by two orders of magnitude. Thus, in order to observe the different behaviors of the effective charges in plasma and cold gas in a laboratory experiment, it matters to have a plasma with high enough areal density.

1.6.2. Dielectronic recombination included [21]

Again we consider the interaction of iodine ion at 1.5 MeV/u with a fully ionized hydrogen plasma at $T = 10$ eV and

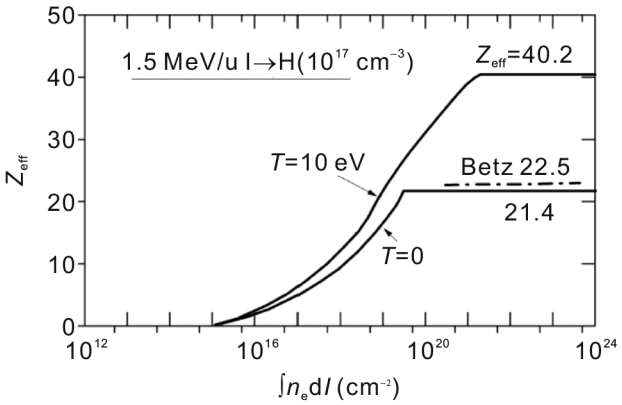

Fig. 7. Time evolution of the effective charge of an iodine beam with 1.5 MeV/u in hydrogen neglecting stopping-power effects. The beam ions have charge zero initially. The dash-dotted line gives the semiempirical value of Betz [*Rev. Mod. Phys.* 44, 465 (1972)] for cold gas.

$n_e = 10^{17}$ cm^{-3}. Now the evaluation of the inflight projectile ion charge state may include simultaneously a DR contribution and the stopping effect, as well (cf. Fig. 8). When the energy loss is not taken into account, $Z_{\mathrm{eff}}(V_p)$ is strongly dependent on the DR rate. This behavior is well documented on Fig. 8 and Table 2 by the constant V_p charge states initialized at $Z_{\mathrm{eff}} = 20$. Asymptotically, i.e. near equilibrium, they climb up to 29 and 41 respectively, with and without DR included. Now, comparing distances for a complete stop, with and without DR included, one gets a ratio $R = 1.17$ for initial charge state 20 and $R = 1.16$ for 32, respectively when stopping is neglected. It has to be appreciated that those R values result only in a 16% DR modification for the complete stopping process. This is 6 times smaller than the ratio 2 of stopping powers pertaining to equilibrium charges $Z_{\mathrm{eq}}(V_p)$ at constant velocity. When stopping is included, the ion projectile is brought to rest at the end of 8 m penetration in the given target plasma. On the other hand, $Z_{\mathrm{eq}}(V_p)$ is obtained only after 40-m penetration depth, when DR is not taken into account. Fig. 8 also displays corresponding evolutions for an initial projectile charge of 32, in between the above two equilibrium values (29 and 41). The

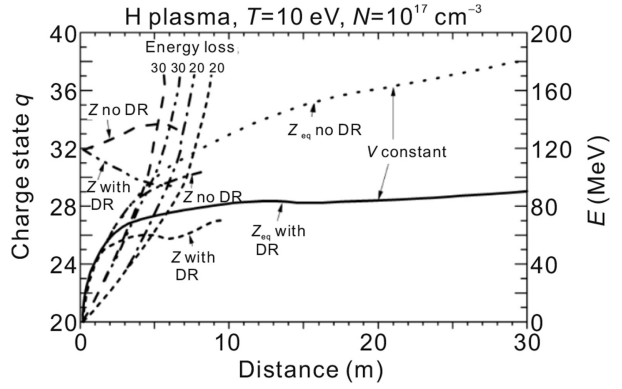

Fig. 8. Variations of projectile ion I^{q+} (initial energy 1.5 MeV/u) charge states in a hydrogen plasma as a function of penetration depth. Reproduced from G. Maynard and C. Deutsch, *Phys. Scr.* 48, 471 (1993) with the permission of IOP Publishing.

main conclusion to be drawn from this detailed investigation is that the realistic interplay of dielectronic recombination and stopping power, likely to be met in an experimental situation, yields a dynamical picture with a rather modest DR impact on the projectile ion effective charge. This statement may be taken as a robust one because we have essentially considered I^{q+} projectile which features one of the highest resonance capabilities to accommodate the DR process [22].

1.7. Inflight effective charge (non-hydrogenic target)

A hydrogen plasma target provides easily a high density of free electrons. However, in order to make contact with realistic stopping plasmas of interest for inertial confinement fusion (ICF) through intense ion beams, one has to consider also high Z and low Z targets of nonhydrogenic materials such as Au, Pb, C, Al, etc.

The corresponding dense and partially ionized plasmas always retain a large amount of bound electrons which contribute significantly to the stopping and also to charge exchange induced electron transfer between incoming partially ionized projectile and target ions in the vicinity of its path. Figs. 9 and 10 display reaction rates weighted by density of excited target bound states for the interaction of Cu^{9+} ions with a hot ($T_e = 250$ eV) Al plasma with a free electron density $n_e = 10^{18}$ cm^{-3}. Fig. 9 features variations in terms of the projectile charge q at 0.781 MeV/u kinetic energy. In Fig. 10 the rate variations are given in terms of projectile Cu^{7+} energy [20].

According to the discussion in Section 1.5 dielectronic recombination may be given for its reaction rate a constant average value $\alpha_{\mathrm{DR}} = 10^{-11}$ cm$^{-3}\cdot$s^{-1}.

This value has been identified as an upper bound (Nardi and Zinamon [6]). Chen's investigations [21] show that α_{DR} remains dependent on target temperature.

The reported variations remain moderate, in particular for a projectile ionization smaller than 10. In order to estimate the final output of those projectile charge variations, we used a parameter study demonstrating that increasing α_{DR} by an order of magnitude or reducing it by the same amount does not change at all the results displayed in Figs. 9 and 10 as well as in experimental cases considered below. In a partially ionized plasma target, the projectile charge state is mostly reached with collisions and charge transfer to target ions. Other free-electron contributions such as dielectronic recombination or three-body recombination are kept three orders of magnitude below the charge transfer once there is 0.5% of bound electrons in the target.

Charge transfer

$$X^{q+} + A^{p+} \rightarrow X^{(q-1)+} + A^{(p+1)+}$$

with the rate a_{qq-1}, features the most important recombination process in neutral gases, solids, or partially ionized plasmas. Nonetheless, in a fully ionized medium, this contribution nearly vanishes. Such a behavior accounts for a drastic reduction of recombination in plasma. Then the result for the

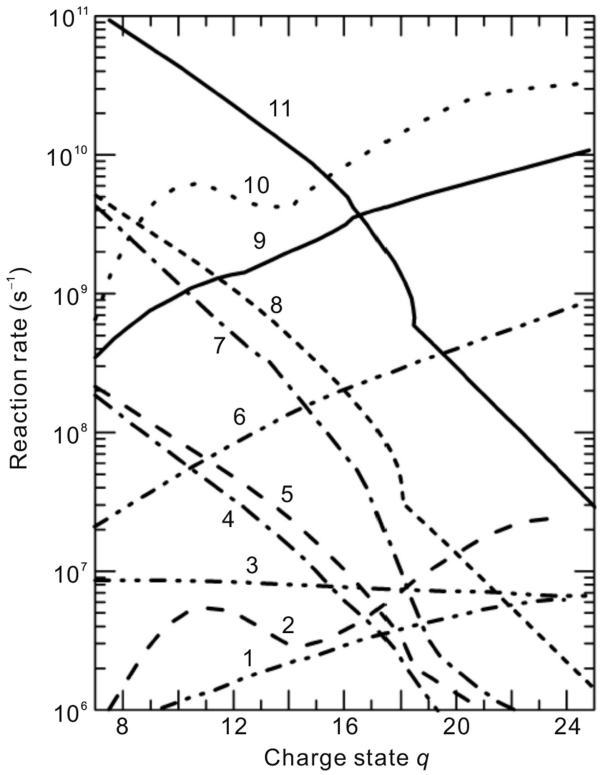

Fig. 9. Reaction rates weighted by density of excited target bound states, versus charge state q, encountered in the interaction of 50 MeV Cu ions with Al plasmas ($T_e = 250$ eV, $n_e = 10^{18}$ cm^{-3}; curves labelling: 1: $n_e\ \alpha_{REC}$; 2: $n(12+)\alpha_{qq-1}$; 3: $n_e\ \alpha_{DR}$; 4: $n(12+)\ \alpha_{ij}$; 5: $n(9+)\alpha_{ij}$; 6: $n(9+)\alpha_{qq-1}$; 7: $n_e\ \alpha_{ie}$; 8: $n(10+)\alpha_{ij}$; 9: $n(10+)\alpha_{qq-1}$; 10: $n(11+)\alpha_{qq-1}$; 11: $n(11+)\alpha_{ii}$. Reproduced from C. Couillaud et al., *Phys. Rev. E* 49, 1545 (1994) with the permission of AIP Publishing.

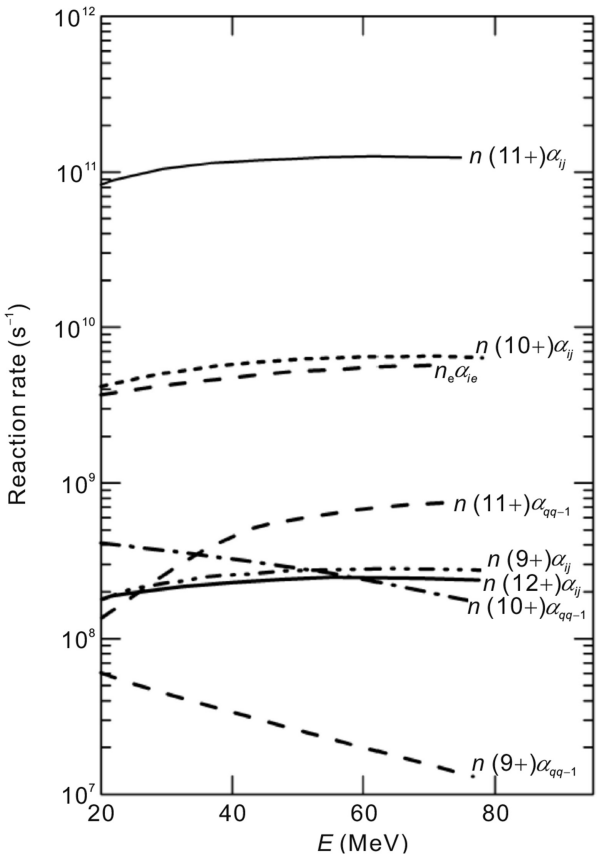

Fig. 10. Reaction rates in the interaction of the 50 MeV Cu^{7+} ions with Al plasmas of Fig. 9 in terms of projectile energy. Other unspecified quantities are as in Fig. 9. Reproduced from C. Couillaud et al., *Phys. Rev.* E 49, 1545 (1994) with the permission of AIP Publishing.

projectile charge is expected to keep same plateau value over most of its velocity range.

Decay by spontaneous emission

$$X^q(E) \rightarrow X^{q+}(E') + h\nu$$

appears non-negligible for highly excited projectiles, while three-body recombination is ruled out because at high projectile velocity and average electron density, conservation of momentum cancels three-body reactions.

In particular, momenta of the two recombining electrons have to compensate each other at the ion location. Such an occurrence decreases very rapidly with increasing projectile velocity (Bailey, Lee and More) [5] (Section 1.2).

As shown above, charge transfer features the most efficient capture process, so a higher projectile charge is expected in a fully ionized plasma than in the equivalent cold gas. Also, for a partially ionized plasma retaining a large number of bound electrons, the projectile equilibrium charge, reached when electron losses balance gains, is seen at higher projectile velocity that in totally stripped plasmas.

In Fig. 9, we picture the above considered reaction rates versus charge state q for the 50-MeV Cu ions interacting with a strongly ionized Al plasma where $T_e = 250$ eV and $n_e = 10^{18}$ cm^{-3}. This target is assumed in a coronal regime with Al^{n+} ions and $n = 9 - 12$.

Excepted the q-independent dielectronic recombination, all other mechanisms are strongly affected by the varying projectile charge state. On the other hand, when that projectile charge state (see Fig. 10) is kept fixed, the corresponding rates remain nearly constant in terms of incoming kinetic energy.

A lot of efforts has been devoted to asserting the actual significance and quantitative relevance of dielectronic recombination on the projectile ion inflight charge state $Z_{eff}(V_p)$, in a strongly ionized target plasma. As a result, the initial picture set forward in Section 1.2 highlighting higher charge states than in equivalent cold gas emerges strengthened by this thorough examination. Hindered recombination actually appears as the trade mark of plasma conditioned projectile effective charge.

Those considerations allow to extract easily the most significant pieces of information encapsulated in Fig. 9. This is performed on Fig. 11. We again consider a Cu^{9+} ion projectile with 50 MeV total kinetic energy, interacting with strongly ionized plasma targets with ion density $= 10^{18}$ cm^{-3}. We restrict to ionizing collisions with target ions and free electrons, as well as to radiative electron capture and 3-body recombination. Projectile excitation is neglected in those simulations.

Fully ionized targets (Fig. 11(a) and (b)) at high temperature exhibit very similar trends, although the first is aluminum and the second carbon. Then, the absence of charge transfer

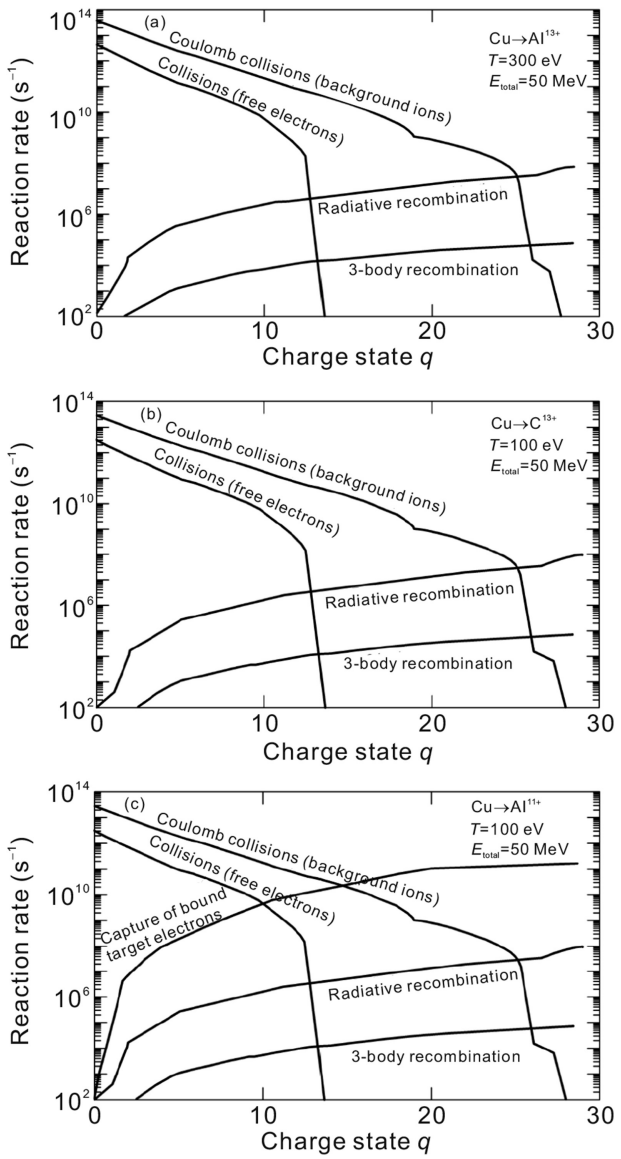

Fig. 11. Reaction rates for 50 MeV Cu ions versus charge state q in the interaction with a plasma (ion density = 10^{18} cm^{-3}). (a) Al at 300 eV (fully ionized), (b) C at 100 eV (fully ionized), and (c) Al at 100 eV.

between target ions and projectile can be observed at top efficiency. However, lowering by a factor of 3 the Al plasma temperature, makes to appear a dominant contribution of recombination through charge transfer. The target ions are then mostly heliumlike with two bound electrons.

2. Stopping by bound electrons

Now, we switch attention to the first term in the right hand side under brackets in Eq. (1). It pertains to the stopping contribution arising from the remaining electrons bound in the partially ionized plasma target. It thus reads as

$$-\frac{\mathrm{d}E}{\mathrm{d}x}=\frac{4\pi\left[Z_{\mathrm{eff}}\left(V_{\mathrm{p}}\right)e^{2}\right]^{2}}{m_{\mathrm{e}}V_{\mathrm{p}}^{2}}n_{\mathrm{T}}\left(Z_{\mathrm{T}}-\overline{Z}\right)\ln\left(\frac{2m_{\mathrm{e}}V_{\mathrm{p}}}{I}\right), \tag{36}$$

in terms of the mean excitation energy

$$\ln(I)=\frac{\sum_{n}f_{n}\ln(E_{n})}{\sum_{n}f_{n}}, \tag{37}$$

where f_n is the dipole oscillator strength for the nth energy level E_n, n_{T} is the ion density in the target. Up to now, most of measurements of the ion stopping have been restricted to cold solid or gaseous targets. In order to optimize the efficiency of a pellet compression, however, an accurate estimation of the stopping parameters in dense and hot plasmas is required. The target material is likely to be heated up to temperatures of 50–200 eV, before fuel ignition starts up in a direct drive approach. Under these conditions, such tamper elements as Pb will be only partially ionized. Consequently, the stopping by bound electrons is no longer negligible and thus, we have to anticipate an energy range of a given ion beam in a cold matter and in an equivalent plasma for the same line density nl (l is the linear projectile range).

The central quantity of present concern is the mean excitation I.

We are thus obviously required to extend to nonhydrogenic cold targets, the usual knowledge already used for neutral atoms and hydrogenic ions. Furthermore, we shall compute the corresponding I in hot and dense plasmas of atomic charge Z_{T}.

Postponing the presentation of low V_{p} behavior we restrict presently to the standard Bethe-Bohr-Bloch regime with $2m_{\mathrm{e}}V_{\mathrm{p}}^{2}/I\geq 1$, i.e

$$MV_{\mathrm{p}}^{2}\geq\frac{M}{m_{\mathrm{e}}}5.15Z_{\mathrm{T}}[\mathrm{eV}]\ ,$$

where Z_{T} now denotes the average nuclear charge in target. Here, we put the main emphasis on theoretical methods which are able to deliver accurate mean excitation energies based on a clear understanding, so that comparison of cold and hot stopping, respectively, for a given ion beam is easily achieved.

This explains why we pay attention to a variational approach yielding upper and lower bounds with a narrow gap in between. Other methods including a cubic spline interpolation, a pseudo-analytic expression for I, and the local plasma approximation (LPA) are also considered.

They all agree in showing that high-temperature plasmas ($k_{\mathrm{B}}T\geq 10$ eV) have significantly smaller mean excitation energies than their cold target homologue.

2.1. Variational method

2.1.1. Sum rules

Starting with a formal approach initiated by Pekeris [23] and Dalgarno [24] and subsequently developed by many authors [25], we consider the sum rules ($-1\leq\mu\leq 2$):

$$S(\mu)=\sum_{n}f_{0n}E_{0n}^{\mu}, \tag{38}$$

$$L(\mu)=\sum_{n}f_{0n}E_{0n}^{\mu}\ln\left|E_{0n}\right|, \tag{39}$$

in terms of optical oscillator strengths ($q\rightarrow 0$ limit),

$$f_{0n} = \frac{2E_{0n}}{N}\left\langle n\left|\sum_{i=1}^{N} Z_i\right|0\right\rangle^2 \text{[a.u.]}, \tag{40}$$

and excitation energy E_{0n} for transitions $\{0\} \rightarrow \{n\}$ in a given atom (ion) with N bound electrons, and nuclear charge Z. Eqs. (38) and (39) interpolate for any $\mu \in [-1, 2]$, the usual physical quantities specified for integer μ. For the sake of simplicity, we restrict our presentation to a one-electron model so that a given subshell $\{\alpha\}$ may be indexed either through classical $\{n, l\}$ or relativistic $\{n, l, j\}$ one-electron quantum numbers. We thus specify Eqs. (38) and (39).

$$S_\alpha(\mu) = \sum_{\alpha'} f_{\alpha\alpha'} E_{\alpha\alpha'}, \tag{41}$$

$$L_\alpha(\mu) = \sum_{\alpha'} f_{\alpha\alpha'} E^{\mu}_{\alpha\alpha'} \ln\left|E_{\alpha\alpha'}\right|. \tag{42}$$

Noticing that an optical transition to an already filled subshell has to be forbidden, we introduce the more realistic sums

$$S^{\mathrm{P}}_\alpha(\mu) = \sum_{\alpha'} (1 - h_{\alpha'}) f_{\alpha\alpha'} E^{\mu}_{\alpha\alpha'}, \tag{41′}$$

$$L^{\mathrm{P}}_\alpha(\mu) = \sum_{\alpha'} (1 - h_{\alpha'}) f_{\alpha\alpha'} E_{\alpha\alpha'} \ln\left|E_{\alpha\alpha'}\right|, \tag{42′}$$

in terms of $h_{\alpha'} = g_{\alpha'}/d_{\alpha'}$, $g_{\alpha'}$ is the number of electrons $\{\alpha'\}$ while $d_{\alpha'}$, refers to level degeneracy, i.e., $2(2l + 1)$ for $\alpha = \{n, l\}$ and $(2j + 1)$ for $\{n, l, j\}$. The overall quantities corresponding to Eqs. (38) and (39) thus read:

$$S^{\mathrm{P}}(\mu) = \sum_{\alpha} g_\alpha S^{\mathrm{P}}_\alpha(\mu), \tag{43}$$

$$L^{\mathrm{P}}(\mu) = \sum_{\alpha} g_\alpha L^{\mathrm{P}}_\alpha(\mu), \tag{44}$$

with:

$$S^{\mathrm{P}}(2k) = S(2k), \quad k \leq 1, \tag{45}$$

$$S^{\mathrm{P}}(2k+1) < S(2k+1), \quad k \leq 1. \tag{46}$$

2.1.2. Upper and lower bounds

We now consider a generalized mean excitation energy under the form:

$$\ln[I(\mu)] = \frac{L^{\mathrm{P}}(\mu)}{S^{\mathrm{P}}(\mu)} = \frac{1}{S^{\mathrm{P}}(\mu)} \frac{\mathrm{d}}{\mathrm{d}\mu} S^{\mathrm{P}}(\mu) \tag{47}$$

The physical I is retrieved in the $\mu = 0$ limit. Now, we turn to the variational procedure itself as considered by Shimamura and Watanabe [26] for an atom in its ground state.

Upper and lower bounds for $\ln[I(\mu)]$ are then deduced from the basic atomic quantities (in a.u.):

$$S_\alpha(-1) = \frac{2}{3}\langle\alpha|r^2|\alpha\rangle = \frac{2}{3} r^2_\alpha, \tag{48a}$$

$$S_\alpha(0) = 1\ , \tag{48b}$$

$$S_\alpha(1) = \frac{4}{3}\left\langle\alpha\left|\left(P^2/2\right)\right|\alpha\right\rangle = \frac{4}{3} K_\alpha, \tag{48c}$$

$$S_\alpha(2) = \frac{1}{3}\left\langle\alpha\left|4\pi Z\delta(r) - \frac{1}{r}\frac{\mathrm{d}^2}{\mathrm{d}r^2}[rV(r)]\right|\alpha\right\rangle, \tag{48d}$$

The operators:

$$P_\alpha = \sum_{\alpha' < \alpha} \sqrt{1 - h_{\alpha'}}\,|\alpha'\rangle\langle\alpha'|$$

and

$$D = \sqrt{2z} = \sqrt{2}(\boldsymbol{q}\cdot\boldsymbol{r}/r) \tag{49}$$

allow us to rephrase Eqs. (41) and (42) under the form ($\alpha' < \alpha$):

$$S_\alpha(\mu) = \left\langle\alpha\left|DP_\alpha(H - E_\alpha)^{\mu+1} P_\alpha D\right|\alpha\right\rangle, \tag{50}$$

$$\mathscr{M}_\alpha(\mu) = \langle\alpha\left|DP_\alpha(H - E_\alpha)^{\mu+1}\ln(H - E_\alpha) P_\alpha D\right|\alpha\rangle, \tag{51}$$

featuring upper and lower bounds straightforwardly deduced from convexity considerations.

Their obvious numerical interest arises from the sharp max-min interval, which allows us to well approximate $\ln(I)$ by the bounds average $\ln\langle I\rangle$ the simplest case of a basis reduced to its first vector u_1. This procedure thus yields

$$\ln\left[\frac{S_\alpha(\mu)}{S_\alpha(\mu-1)}\right] \leq \frac{\mathscr{M}_\alpha(\mu)}{S_\alpha(\mu)} \leq \ln\left[\frac{S_\alpha(\mu+1)}{S_\alpha(\mu)}\right] \tag{52}$$

2.1.3. Analytic formula

For an ion (atom) in its ground state, Eq. (52) reduces to

$$\ln\left[\frac{S^{\mathrm{P}}(\mu)}{S^{\mathrm{P}}(\mu-1)}\right] \leq \frac{L^{\mathrm{P}}(\mu)}{S^{\mathrm{P}}(\mu)} \leq \ln\left[\frac{S^{\mathrm{P}}(\mu+1)}{S^{\mathrm{P}}(\mu)}\right] \tag{53}$$

because there is no superelastic transition. $S^{\mathrm{P}}(\mu)$ fulfills

$$S^{\mathrm{P}}(0) = S(0),\ S^{\mathrm{P}}(1) < S(1),\ S^{\mathrm{P}}(-1) < S(-1). \tag{54}$$

In the $\mu = 0$ limit one gets:

$$\ln\left[\frac{S(0)}{S(-1)}\right] \leq \ln(I) \leq \ln\left[\frac{S(1)}{S(0)}\right]. \tag{55}$$

Taking the bounds average leads to

$$\ln\langle I\rangle = \frac{1}{2}\ln\left[\frac{S(1)}{S(-1)}\right] \tag{56}$$

which compares very well with the Hartree-Fock-Slater (HFS) results given by Dehmer, Inokuti and Saxon [27] (DIS).

Estimate (56) is the basis for variational results plotted in Figs. 4–6 together with the HFS ones. Neglecting correlations between bound electrons allows us to use (a_0 = Bohr radius)

$$S(-1) = \frac{2m_{\mathrm{e}}}{3\hbar^2} a_0^2 \left\langle\left(\frac{r}{a_0}\right)^2\right\rangle_0, \tag{57a}$$

$$S(1)=\frac{4}{3}K_0, \tag{57b}$$

which, when introduced into Eq. (55) yield the explicit form:

$$\langle I\rangle=\sqrt{\frac{2K_0}{r_0^2}}\ [\text{a.u.}], \tag{58}$$

with $r_0^2=\langle r^2\rangle_0$.

This novel approximation already provides a very good estimate for I. The practical interest of Eq. (58) would remain rather limited if one could only proceed to a sophisticated evaluation for K_0 and r_0^2. Hopefully, these quantities are easily deduced from electron-ion pseudo-analytic effective interactions which enables us to compute these parameters with the same accuracy.

As experienced earlier, we find it convenient to explain these effective interactions in the GSZ form [28]

$$V(r)=-\left(\frac{Z_{\rm T}-N+1}{r}\right)\varphi(r), \tag{59a}$$

$$\varphi(r)=-\left(\frac{N-1}{r}\right)\Omega(r), \tag{59b}$$

$$\Omega(r)=\left[H\left(\mathrm{e}^{r/d}-1\right)+1\right]^{-1}. \tag{59c}$$

H and d denote two adjustable parameters fitted on the lowest bound state energies.

For our present goals, the quantity of interest is the electron density $\rho(r)$ fulfilling the Poisson equation,

$$\nabla^2\varphi(r)=-4\pi\rho(r),$$

with

$$4\pi r^2\frac{\rho(r)}{N}=\frac{H}{d^2}r\mathrm{e}^{r/d}\frac{H\left(\mathrm{e}^{r/d}+1\right)-1}{\left[H(\mathrm{e}^{r/d}-1)+1\right]^3}. \tag{60}$$

From Eq. (60) one readily obtains

$$\int_0^R r^2 4\pi r^2\rho(r)\mathrm{d}r=-\int_0^R\left(r^2\frac{\mathrm{d}}{\mathrm{d}r}\right)\left(r^2\frac{\mathrm{d}\varphi}{\mathrm{d}r}\right)\mathrm{d}r$$

$$=\left(r^4\frac{\mathrm{d}\varphi}{\mathrm{d}r}\right)_0^R+\left(2r^3\varphi\right)_0^R-6\int_0^R r^2\varphi(r)\mathrm{d}r$$

through an integration by parts, so ($R\to\infty$),

$$Nr_0^2=-6\int_0^\infty \mathrm{d}r\cdot r^2\varphi(r)=r_{\rm G}^2F(\alpha),\quad \alpha=1-1/H, \tag{61}$$

where $r_{\rm G}^2=6Nd^2/H$ and

$$F(\alpha)=\sum_{n=0}^{\infty}\frac{\alpha^n}{(n+1)^2}$$

with $0\le\alpha\le 1$.

The average kinetic energy K_0 is reached through a constrained virial relationship:

$$2K_0\cong-\frac{\langle V\rangle}{N}=-\frac{U}{N}$$

$$-\frac{1}{N}\int_0^\infty\left[-\left(\frac{Z_{\rm T}-N+1}{r}\right)\left(\frac{N-1}{r}\right)\frac{1}{H(\mathrm{e}^{r/d}-1)+1}\right]4\pi r^2\rho(r)\mathrm{d}r$$

$$=\frac{NH}{d}\left[Z-N\left(\frac{1}{6}+\frac{1}{12H}\right)\right]. \tag{62}$$

Finally, putting Eqs. (61) and (62) into Eq. (57) yields the Garbet expression [29]

$$\langle I\rangle^2=\frac{N}{6d}\left(\frac{H}{d}\right)^2\frac{\left[1-\left(\frac{N}{6Z}\right)\left(1+\frac{1}{2H}\right)\right]}{F\left(1-\frac{1}{H}\right)}. \tag{63}$$

If we now specify the above results to the neutral atom limit ($Z_{\rm T}=N$) and recall the empirical estimate

$$I\cong 10.32\ [\text{eV}], \tag{64}$$

one expects a behavior $\langle I\rangle\cong Z_{\rm T}$, arising from the GSZ scaling law [28]

$$\frac{H}{d}=Z_\beta,\quad \beta=0.5. \tag{65}$$

This result is indeed confirmed when the Thomas-Fermi estimates $NK_0\sim Z_{\rm T}^{7/3}$ and $Nr_0^2\sim Z_{\rm T}^{1/2}$ are introduced into Eq. (58). The corresponding $\langle I\rangle$ falls within 6% of DIS ones [27] for $Z_{\rm T}\ge 28$ (see Fig. 12). Putting Eq. (65) into Eq. (63) yields

$$\langle I\rangle^2=\frac{Z_{\rm T}N}{6d}\frac{\left[1-\left(\frac{N}{6Z}\right)\left(1+\frac{1}{H}\right)\right]}{F\left(1-\frac{1}{H}\right)}, \tag{66}$$

with the atomic limit ($Z_{\rm T}=N$)

$$\langle I\rangle^2=\frac{Z_{\rm T}^2}{6d}\frac{9+\alpha}{12F(\alpha)}. \tag{67}$$

In the TF limit ($Z\to\infty$), one has

$$\alpha=1,\quad F(\alpha)=\frac{\pi^2}{6},$$
$$\frac{\langle I\rangle}{Z_{\rm T}}=\sqrt{\frac{5}{6\pi^2 d}}, \tag{68}$$

which when combined to the most likely estimated $d/a_0\sim 0.7$, provides

$$\frac{\langle I\rangle}{Z_{\rm T}}\cong 9.4462\ \left[\text{eV}\right] \tag{69}$$

in fair agreement with Eq. (64). The main interest of Eq. (63) lies in its flexibility. It applies to any ionicity (see Fig. 13) and to arbitrarily partially stripped ions in plasmas.

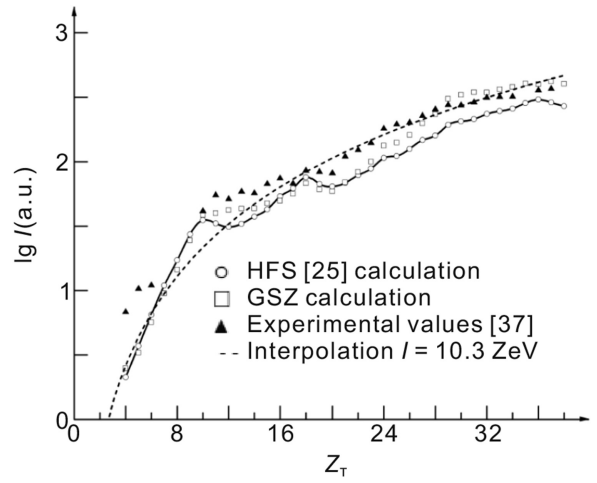

Fig. 12. Mean excitation energies for neutral species ($1 \leq Z_T \leq 40$). Reproduced from X. Garbet et al., *J. Appl. Phys.* 61, 907 (1987) with the permission of AIP Publishing.

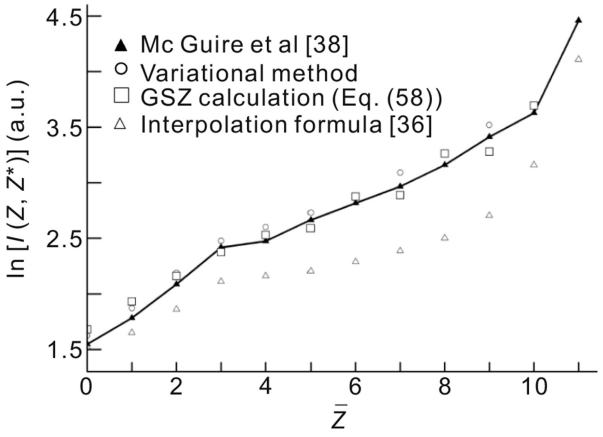

Fig. 13. Mean excitation energies for isolated ion Al^{n+} according to ionicity. Reproduced from X. Garbet et al., *J. Appl. Phys.* 61, 907 (1987) with the permission of AIP Publishing.

2.2. Cubic spline method

Here we essentially show how some variational results can improve a spline interpolation method initially worked out by Peek et al. [30]. For this purpose, let us reconsider Eq. (47) with the P superscript deleted, under the form

$$\ln(I) = \frac{\mathrm{d}}{\mathrm{d}\mu}\ln[S_\alpha(\mu)]\Big|_{\mu=0}, \tag{70}$$

which suggests a numerical interpolation by considering real μ values, provided the integer data $\mu = -1$, 0, 1 and 2 are known. Arguing that $S(\mu)$ diverges logarithmically at $\mu = 2.5$, Dalgarno [24] has considered the formula

$$S(\mu) = \left[a + b\mu + c\mu^2 + d\mu\ln(2.5-\mu)\right]^{\mu} S(0),$$

where a, b, c, d are suitable constants prescribed by specific constraints. These techniques have been further [31] taken up by specifying Eq. (46) to a subshell α, with

$$\ln(I_\alpha) = \frac{\mathrm{d}}{\mathrm{d}\mu}\ln[S_\alpha(\mu)]\Big|_{\mu=0},$$

and the interpolation formula

$$\ln\left[\frac{S_\alpha(\mu)}{S_\alpha(0)}\right] = \mu\left(a + \frac{b}{5-2\mu} + \frac{c}{7-2\mu}\right),$$

where a, b, c are another set of disposable parameters. Setting

$$T_\alpha(\mu) = \frac{1}{\mu}\ln\left[\frac{S_\alpha(\mu)}{S_\alpha(0)}\right],$$

$\ln(I_\alpha)$ becomes

$$\ln(I_\alpha) = \frac{3}{5}T_\alpha(-1) + \frac{3}{7}T_\alpha(1) - \frac{1}{35}T_\alpha(2).$$

2.3. Ions in plasma

2.3.1. Average atom model

With the obvious intention of extending the scope of the above methods to the plasma case, we implement a scheme proposed by Rozsnayi [32]. It usually leads to results close to those of the Liberman [33] average atom model.

This is essentially an algorithm delivering electronic levels and equation of state of atoms embedded in matter with arbitrary density and temperature.

The self-consistent field treatment starts with the relativistic Thomas-Fermi-Dirac (TFD) model in the iterative procedure.

The Fermi statistics and the central field approximation are maintained, giving an average atom representation. It is generally believed that in the region of high temperature and/or pressure, the TFD model gives a reasonably accurate electron potential. This potential, in turn, can be used as a basis to treat the atom in a more quantum-mechanical way by solving the single-electron wave equation for the bound states.

The basic assumption is that during an elementary stopping process, the target ion is nearly instantaneously neutralized by plasma fluctuations. This hypothesis is particularly relevant to matter treated by intense ion beams, in view of the relatively long pulse time (~20 − 30 ns) allowing the target species to be considered in local thermodynamic equilibrium (LTE) with comparable electron and ion temperature T and number density n.

The numerical procedure is initialized by taking each $R_0 = (3/4\pi n)^{1/3}$. According to Rozsnayi [32] the HFS scheme is implemented as follows.

1. Bound electrons are consider independent. They are supposed to be modeled in spherically symmetric and self-consistent potential $V_{\mathrm{eff}}(r)$ (see Eq. (73) below), the same for all electrons. However, exchange and correlation are still retained in $V_{\mathrm{eff}}(r)$. The total electron density:

   $$\rho(r) = \rho_{\mathrm{b}}(r) + \rho_{\mathrm{f}}(r),$$

   fulfills

$$4\pi \int_0^{R_0} \mathrm{d}r \bullet r^2 \rho(r) = Z_{\mathrm{T}}, \tag{71}$$

with $\rho_{\mathrm{b}}(r)$ in terms of single-electron eigenquantities (ε_i, Ψ_i).

2. The average atom assumption allows us to replace the various excitation states in target with those of a fictitious atom with noninteger occupation numbers for excited orbitals. $V_{\mathrm{eff}}(r)$ is taken constant within each subshell.
3. Conceptually and numerically speaking it is most convenient to derive (ε_i, Ψ_i) from Dirac equation, which proves especially convenient to tackling the eigenvalue problem through two coupled first-order equations.

   We do not intend to emphasize relativistic and spin effects of increasing relevance for heavy elements. However, this could be easily done within the present framework.
   The bound electron radial density $\rho_{\mathrm{b}}(r)$

$$4\pi\rho_{\mathrm{b}}(r) = \sum_{nlj} \frac{(2j+1)}{\exp\left[\beta\left(E_{nlj}-\mu\right)\right]+1} \times \left[A^2_{nlj}(r) + B^2_{nlj}(r)\right], \tag{72}$$

   with total electron energy

$$E'_{nlj} = E_{nlj} + V_{\mathrm{eff}}(r),$$

   and

$$V_{\mathrm{eff}}(r) = V_{\mathrm{cb}}(r) + V_{\mathrm{exch}}(r) + V_{\mathrm{cor}}(r), \tag{73}$$

   a sum of Coloumb, exchange, and correlation potentials is readily expressed in terms of radial Dirac wave functions deduced from

$$\frac{\mathrm{d}}{\mathrm{d}r}\begin{pmatrix} A \\ B \end{pmatrix} = \begin{pmatrix} -\dfrac{K}{r} & \dfrac{V_{\mathrm{eff}}(r)-E_{nlj}}{cs} \\ -\dfrac{V_{\mathrm{eff}}(r)-E_{nlj}}{cs} & \dfrac{K}{r} \end{pmatrix}\begin{pmatrix} A \\ B \end{pmatrix}, \tag{74}$$

   where $K = -s(j+l/2)$, $\quad c = 137.037$ (a.u.), $\quad s = \pm 1$.

4. The free electron density is taken to be Thomas-Fermi like i.e.,

$$\rho_f(r) = \frac{\sqrt{2}}{\pi^{3/2}} T^{3/2} \int_{-\frac{V_{\mathrm{eff}}(r)}{K_{\mathrm{B}}T}}^{\infty} \frac{x^{1/2}\mathrm{d}x}{\exp\left\{x - \frac{\left[\mu - V_{\mathrm{eff}}(r)\right]}{K_{\mathrm{B}}T}\right\}+1}, \tag{75}$$

   with the boundary condition $V_{\mathrm{eff}}(R_0) = 0$. E_{nl} is devided from the Wigner-Seitz condition $\Psi(R_0) = 0$.

5. The number $\overline{Z}(n,T)$ of free electrons per nuclei in target may be initialized with a Thomas-Fermi approximation.
6. It appears convenient to initialize $V_{\mathrm{eff}}(r)$ with (see Eq. (59))

$$V_0(r) = \frac{Z_{\mathrm{T}} - \overline{Z}}{r}\Omega(r) = \frac{\overline{Z}}{R_0}\left[\frac{R_0}{r} + \frac{1}{2}\left(\frac{r}{R_0}\right)^2 - \frac{3}{2}\right], \tag{76}$$

   a superposition of GSZ (bound) and ion-sphere potential (free), allowing for a self-consistent resolution of the TF model. (ε_i, Ψ_i) are also initialized by their WKB values.

Table 3
Average Al atom in plasma with $T = 100$ eV (3.657 a.u.) at the three densities (a) $\rho = 0.1\ \rho_0$, (b) $\rho = \rho_0$, and (c) $\rho = 10\rho_0$, with $\rho = 2.699\ \mathrm{g\cdot cm^{-3}}$, solid density. Occupation numbers (usually noninteger) and eigenvalues are plotted for the successive (orbitals) subshells $(n,\ l,\ j)$. Variational outputs for $S^{\mathrm{p}}(0)$, $S^{\mathrm{p}}(1)$, and $S^{\mathrm{p}}(2)$ together with mini-max for $L^{\mathrm{p}}(0)$ and $L^{\mathrm{p}}(1)$ are given, with the corresponding K_0 and $\langle r^2\rangle_0$ required to implement GSZ expression (58). Chemical potential μ, bound electrons number N, and free electron number $\overline{Z}(N+\overline{Z}=Z_{\mathrm{T}})$ are also displayed.

(a) $\rho = 0.1\rho_0$, $R_0 = 6.44$ a.u.

Orbitals	Electrons occupation number	Hamiltonian eigenvalue	
$1s^1_2$	2.000	−69.453	$S^{\mathrm{p}}(-1) = 1.947$
$2s^1_2$	0.391	−12.307	$S^{\mathrm{p}}(0) = 4.056$
$2p^2_2$	0.331	−11.560	$S^{\mathrm{p}}(1) = 2.391 \times 10^2$
$2p^3_2$	0.657	−11.528	$S^{\mathrm{p}}(2) = 1.275 \times 10^5$
$3s^1_2$	0.042	−3.3995	$K_0 = 46.81$
$3p^1_2$	0.039	−3.1300	$\langle r^2\rangle_0 = 0.733$
$3p^3_2$	0.078	−3.1209	
$3d^3_2$	0.072	−2.8112	
$3d^5_2$	0.108	−2.8044	
$4s^1_2$	0.021	−0.8836	
$4p^1_2$	0.021	−0.7737	
$4p^3_2$	0.042	−0.7707	
$4d^3_2$	0.040	−0.6494	
$4d^5_2$	0.060	−0.6161	
$4f^7_2$	0.079	−0.5872	
$4f^5_2$	0.058	−0.4926	
$5s^1_2$	0.017	−0.0755	

$\mu = -1.751$; $N = 4.06$; $\overline{Z} = 8.94$;
$14.83 \le L^{\mathrm{p}}(0) \le 15.08$; $2.529 \times 10^3 \le L^{\mathrm{p}}(1) \le 2.718 \times 10^3$

(b) $\rho = \rho_0$, $R_0 = 2.99$ a.u.

Orbitals	Electrons occupation number	Hamiltonian eigenvalue	
$1s^1_2$	2.000	−63.951	$S^{\mathrm{p}}(-1) = 3.004$
$2s^1_2$	0.792	−8.3632	$S^{\mathrm{p}}(0) = 5.777$
$2p^1_2$	0.667	−7.3733	$S^{\mathrm{p}}(1) = 2.515 \times 10^2$
$2p^3_2$	1.327	−7.3450	$S^{\mathrm{p}}(2) = 1.342 \times 10^5$
$3s^1_2$	0.154	0.7896	$K_0 = 35.90$
$3p^3_2$	0.290	−0.5509	$\langle r^2\rangle_0 = 0.828$
$3p^1_2$	0.140	−0.4078	
$3d^5_2$	0.407	−0.2823	

$\mu = -9.916$; $N = 5.78$; $\overline{Z} = 7.22$;
$18.29 < L^{\mathrm{p}}(0) < 19.31$; $2.589 \times 10^3 \le L^{\mathrm{p}}(1) \le 2.825 \times 10^3$

(c) $\rho = 10\rho_0$, $R_0 = 1.39$ a.u.

Orbitals	Electrons occupation number	Hamiltonian eigenvalue	
$1s^1_2$	2.000	−57.335	$S^{\mathrm{p}}(-1) = 1.139$
$2s^1_2$	1.252	−3.4574	$S^{\mathrm{p}}(0) = 6.528$
$2p^3_2$	2.214	−2.3550	$S^{\mathrm{p}}(1) = 2.507 \times 10^2$
$2p^1_2$	1.062	−2.0194	$S^{\mathrm{p}}(2) = 1.272 \times 10^5$
			$K_0 = 31.86$
			$\langle r^2\rangle_0 = 0.340$

$\mu = -1.565$; $N = 6.53$; $\overline{Z} = 6.47$
$20.32 \le L^{\mathrm{p}}(0) \le 22.20$; $2.536 \times 10^3 \le L^{\mathrm{p}}(1) \le 2.814 \times 10^3$

7. Once convergence is reached, these eigenquantities are self-consistently determined for a given set (n,T) of plasma conditions, together with definitive expressions for $V_{\rm eff}$, $\mu(n,T)$ and $n_{\rm e}$ (see Table 3 for illustration).

2.3.2. Mean excitation energies in plasmas

To illustrate the whole procedure, let us compare $\langle I\rangle$ in Al plasma and for an isolated Al^{3+} ion, respectively, according to Eq. (56). In the first option, we take $K_{\rm B}T = 100$ eV and $n = 10$ solid density, so that (in a.u.)

$$K_0 = 22.42, \quad r_0^2 = 0.493, \quad \overline{Z} = 3$$

leads to $\langle I\rangle = 2.255$ slightly overshooting the more accurate (variational) data 2.16. The corresponding isolated ion results are

$$K_0 = 24.79, \quad r_0^2 = 0.341, \quad \langle I\rangle = 2.49$$

in lieu of the exact 2.48.

On Figs. 14 and 15, we have also reported data due to the local plasma approximation (LPA) [34]. The LPA consists of averaging over density of the inhomogeneous fluid of bound electrons around a target ion.

Despite its obvious plasma connotation, this method provides results among the least accurate, according to ($\gamma = 2$),

$$\ln(I) = \int \ln\left[\gamma\hbar\omega_{\rm p}(r)\right]\rho_{\rm b}(r){\rm d}r \tag{77}$$

with

$$\omega_{\rm p}^2(r) = 4\pi\rho_{\rm b}(r)e^2/m_{\rm e}.$$

We recall that accuracy of these theoretical results in cold matter is evaluated with respect to those of DIS [27] which are *ab initio* HFS.

The present bleak performances of the LPA even at room temperature, are not completely unexpected [35] in view of the basic difficulties encountered when one tries to derive this scheme from the first principles, i.e, starting with the standard definition of the oscillator strength in terms of dipole matrix elements and carrying out a systematic deduction. This point and many others concerning the LPA have recently been critically reviewed by Johnson and Inokuti [35].

In this connection, it should be appreciated that our present results reinforce the paradoxical status of the LPA because it is supposed to be precisely at its best in yielding accurate I values. Nonetheless, we have described three other methods which are easily accurate in cold matter, where contact can be performed with the most accurate DIS ones [27].

The above atomic methods detailed in Sections 2.1 and 2.2 for isolated species are thus renormalized with plasma effects according to Section 2.3.

Their respective $\ln I$ (I in a.u.) are contrasted in Figs. 7 and 8 for Al at various densities and Fe. All the results agree in showing

$$I(Z_{\rm T}, n, T > 10\ [{\rm eV}]) < I\left[Z_{\rm T}, \overline{Z}(n,T)\right] \tag{78}$$

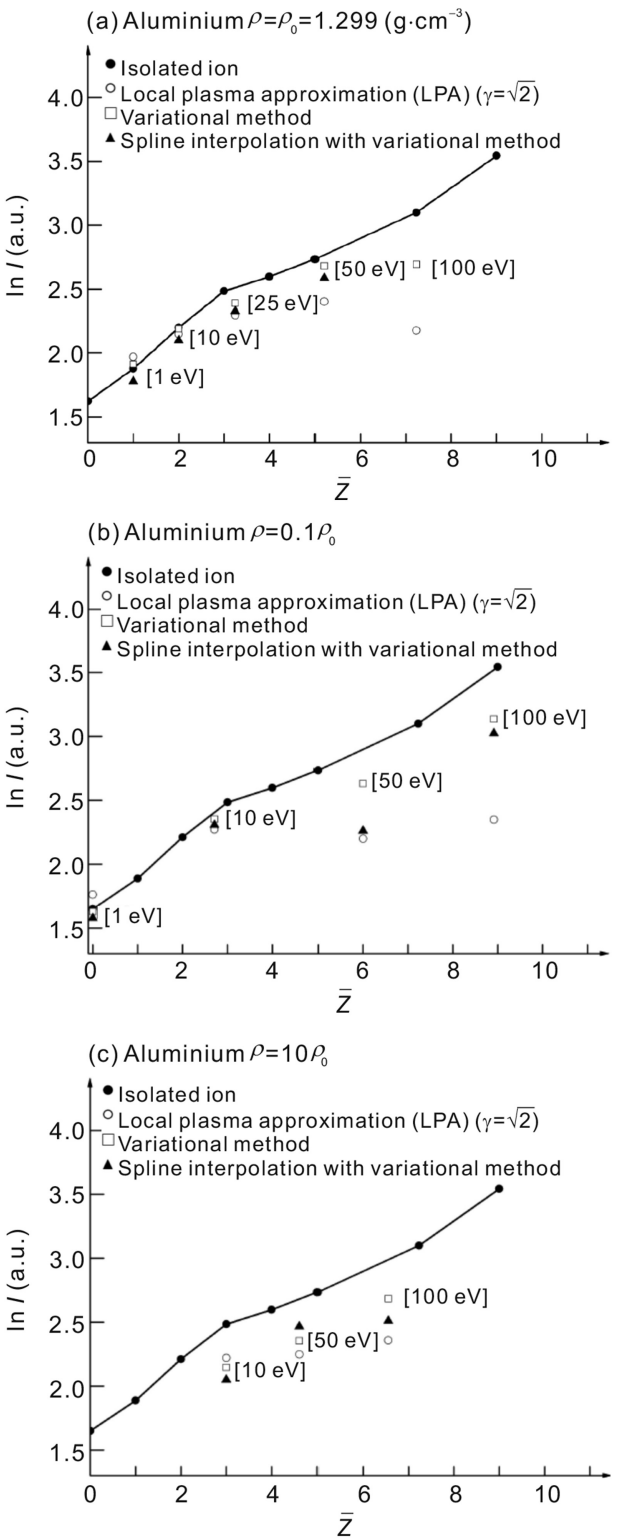

Fig. 14. Mean excitation energies for Al in a hot plasma at (a) solid density, (b) 0.1 × solid density, (c) 10 × solid density. Reproduced from X. Garbet et al., *J. Appl. Phys.* 61, 907 (1987) with the permission of AIP Publishing.

Up to a temperature of 10 eV, it is acceptable to deduce I from a Saha determination of ionization $\overline{Z}$ in target. However, at a higher temperature, occupation of higher subshells has to be taken into account, and their contribution to stopping is larger than that arising from more tightly bound electrons in

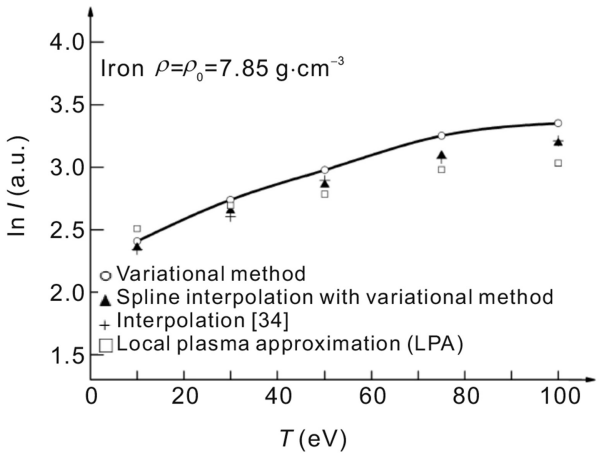

Fig. 15. Mean excitation energies in Fe plasma at solid density, as a function of temperature. Reproduced from X. Garbet et al., *J. Appl. Phys.* 61, 907 (1987) with the permission of AIP Publishing.

lower subshells. The spline interpolation adequately improved with variational inputs seems to provide fair data. As stated, the LPA produces the least accurate results.

At this juncture, it has to be appreciated that the accuracy of the variational results is not restricted by the numerical procedure. For instance, the mesh used for computing the basis wave functions may be taken as densely as required. The variational accuracy is mostly limited by neglecting of any electron exchange between neighboring ions. As shown in Tables 3 and 4 variational results can be given with controlled accuracy, when compared to those of other methods [36]. Finally, we display in Table 4 corresponding variational results for an average Al (Tables 3 and 4) atom in dense hot matter. As stressed above, the excited subshells have a noninteger occupation number.

The present calculations clearly exhibit the temperature limit above which the isolated ion approximation implemented with Saha distribution of excited states, has to be questioned. Through the AAM the plasma effects result in a larger population of excited bound orbitals, which respond more efficiently to the projectile field than corresponding ground state [37,38].

Table 4
$\ln(I)$ (I in a.u.) for isolated ion Al^{n+}. Maximum discrepancy for the variational results are given within parentheses.

Ionicity	McGuire [36]	GSZ [Eq. (58)]	Variational method	Mehlhorn [34]
0	1.51	1.51	1.61 (7.0%)	1.52
1	1.77	1.91	1.87 (4.5%)	1.65
2	2.11	2.13	2.16 (4.2%)	1.85
3	2.44	2.39	2.47 (3.5%)	2.10
4	2.48	2.53	2.59 (3.0%)	2.15
5	2.66	2.58	2.72 (2.7%)	2.20
6	2.82	2.75	2.87 (3.2%)	2.28
7	2.97	2.88	3.04 (3.2%)	2.37
8	2.16	3.04	3.24 (3.0%)	2.50
9	3.40	3.26	3.51 (2.9%)	2.71
10	3.82	3.68		3.15
11	4.47			4.10

The results add a novel and significant contribution to the shortening of the projectile range in target, in addition to those due to partial degeneracy of the electron fluid and enhanced projectile charge in plasma [37] already considered previously.

3. Nonlinear stopping

Up to now, we restricted our investigations to the standard stopping model (SSM) framework and to a first term $\sim Z_{\rm eff}^2(V_{\rm p})$ in the interaction expansion. Nonetheless, for completeness and above all to secure the quantitative pertinence of the above results, it appears compulsory to pay detailed attention to the higher and so-called nonlinear corrections to the usual Bohr-Bethe quadratic dependence in the projectile charge of the stopping power expression. A lot of attention has already been given to those terms for the usual case of a gaseous target [39]. Our main concern here is to adapt these results to a noneutral target by revisiting the corresponding formalisms.

In order to focus attention on the stopping mechanisms, we take it here for granted that the ion projectile keeps a fixed inflight charge $Z_{\rm p}$. We therefore pay a first attention to the so-called Barkas contribution [39] $Z_{\rm p}^3$.

It is also the first nonlinear stopping contribution which now depends on the $Z_{\rm p}$ sign.

3.1. Barkas effect

3.1.1. Classical formulation

The theoretical framework considered up to now is essentially based on the first Born approximation in which the stopping power for a particle of velocity $V_{\rm p}$ energy, and charge number $Z_{\rm p} \ll V_{\rm p}/V_0$, where $V_0 = e^2/\hbar$ is proportional to $(Z_{\rm p}e)^2$. This section extends the stopping-power theory to the term $\cong (Z_{\rm p}e)^2$ in an impulse approximation, i.e., the classical equivalent of the second Born approximation. It accounts for the observed differences between the electromagnetic stopping power of a particle and its antiparticle, and also for differences between the stopping powers of α particles and protons which, so far, have remained unexplained.

Consider first an electron bound harmonically with a frequency ω to the nucleus of the atom in a target with atoms of atomic number $Z_{\rm T}$ and density $n_{\rm T}$. A heavy projectile of charge $Z_{\rm p}e$ approaches the oscillator with non relativistic velocity $V_{\rm p}$ at an impact parameter b relative to atom nucleus. $f(t,b)$ denotes the classically force on the electron set up by the projectile at time t. The displacement of the electron at time t from its equilibrium position (at the origin with zero velocity at $t = -\infty$), $\boldsymbol{\zeta}(t)$, is then obtained through $\ddot{\boldsymbol{\zeta}} + \omega^2\boldsymbol{\zeta} = \frac{\boldsymbol{f}}{m_{\rm e}}$, which we write in the form [39].

$$\boldsymbol{\zeta}(t) = \mathrm{Re}\left[\frac{\mathrm{i}}{m_{\rm e}\omega}\int_{-\infty}^{t}\boldsymbol{f}(t',b)\mathrm{e}^{-\mathrm{i}\omega(t-t')}\mathrm{d}t'\right]. \tag{79}$$

At time t, the electron gained the energy $\frac{1}{2}m_{\rm e}(\dot{\zeta}^2 + \omega^2\zeta^2)$. Thanks to Eq. (79), this energy is given by

$$W_{\mathrm{r}}(t,b)=\frac{1}{2m}\left|\int_{-\infty}^{t}\boldsymbol{f}(t',b)\mathrm{e}^{-\mathrm{i}\omega t'}\mathrm{d}t'\right|^{2}. \tag{80}$$

Thus the energy lost by the incident particle per unit distance dR, i.e., the stopping power of the fraction F_ω of target electrons bound with a frequency ω, appears as:

$$\left(-\frac{\mathrm{d}E}{\mathrm{d}x}\right)_{\omega}=2\pi n_{\mathrm{T}}Z_{\mathrm{T}}F_{\omega}\left[\int_{0}^{a_\omega}b\mathrm{d}bW_{\mathrm{S}}(\infty,b)+\int_{a_\omega}^{\infty}b\mathrm{d}bW_{\mathrm{r}}(\infty,b)\right], \tag{81}$$

where W_{r} is the energy transferred to resonance excitations of the electrons and W_{S} is the energy transferred in close single collisions. a_ω advocates a lower limit of the impact parameter with the electrons seen as harmonically bound. For $b<a_\omega$ the electrons are treated as unbound. If the incident particle moves along the line $x=-b$ in the $+y$ direction, the force (see Fig. 16) on the electron can be written with Eq. (79) as:

$$\boldsymbol{f}(t,b)=-Z_{\mathrm{p}}e^{2}\frac{[b+\zeta_x(t)]\hat{\boldsymbol{i}}-[V_{\mathrm{p}}t-\zeta_y(t)]\hat{\boldsymbol{j}}}{\left\{[b+\zeta_x(t)]^{2}+[V_{\mathrm{p}}t-\zeta_y(t)]^{2}\right\}^{3/2}} \tag{82}$$

where $\hat{\boldsymbol{i}}$ and $\hat{\boldsymbol{j}}$ are unit vectors in the $+x$ and $+y$ directions. For small electron displacements such that $\zeta(t)/(b^2+V_{\mathrm{p}}^2t^2)^{1/2}\ll 1$ and retaining first-order terms, one gets:

$$\boldsymbol{f}(t,b)=\boldsymbol{f}_0(t,b)+\Delta\boldsymbol{f}(t,b) \tag{83}$$

where $\boldsymbol{f}_0(t,b)$ denotes the standard expression:

$$\boldsymbol{f}_0(t,b)=-Z_{\mathrm{p}}e^{2}\frac{b\hat{\boldsymbol{i}}-V_{\mathrm{p}}t\hat{\boldsymbol{j}}}{\left[b^{2}+\left(V_{\mathrm{p}}t\right)^{2}\right]^{3/2}}. \tag{84}$$

The new term $\Delta\boldsymbol{f}$ is explained as:

$$\begin{aligned}\Delta\boldsymbol{f}(t,b)=-\frac{Z_{\mathrm{p}}e^{2}}{\left[b^{2}+\left(V_{\mathrm{p}}t\right)^{2}\right]^{5/2}}\Big\{\Big[\Big(-2b^{2}+V_{\mathrm{p}}^{2}t^{2}\Big)\zeta_x(t)\\+3bV_{\mathrm{p}}t\zeta_y(t)\Big]\hat{\boldsymbol{i}}+\Big[3bV_{\mathrm{p}}t\zeta_y(t)\\+\Big(b^{2}-2V_{\mathrm{p}}^{2}t^{2}\Big)\zeta_y(t)\Big]\hat{\boldsymbol{j}}\Big\}.\end{aligned} \tag{85}$$

Solving Eq. (83) iteratively and, replacing $\boldsymbol{f}$ by $\boldsymbol{f}_0$ when calculating $\boldsymbol{\zeta}(t)$ from Eq. (79), we insert the Fourier transforms $\boldsymbol{f}_{0\omega}$ and $\Delta\boldsymbol{f}_\omega$ into $W_{\mathrm{r}}(\infty,b)$, yielding Eq. (80) the stopping-power correction due to $\Delta\boldsymbol{f}$, i.e

$$\begin{aligned}\Delta\left(-\frac{\mathrm{d}E}{\mathrm{d}x}\right)_{\omega}=\frac{2\pi n_{\mathrm{T}}Z_{\mathrm{T}}F_{\omega}}{m_{\mathrm{e}}}\int_{a_\omega}^{\infty}b\,\mathrm{d}b(\mathrm{Re}\boldsymbol{f}_{0\omega}\cdot\mathrm{Re}\Delta\boldsymbol{f}_{\omega}\\+\mathrm{Im}\boldsymbol{f}_{0\omega}\cdot\mathrm{Im}\Delta\boldsymbol{f}_{\omega}).\end{aligned} \tag{86}$$

The dipole approximation implied in Eq. (86) limits its validity range to distances from nucleus outside the atomic volume so that the electrons responding with frequency ω remain bound. This restricts a_ω to values larger than the respective shell radius. For smaller impact parameters the momentum transfer becomes so large that the electrons turn quasi-free and their contribution to the Z_{p}^3 effect becomes small, because the cross section for Rutherford scattering with free electrons is exactly proportional to Z_{p}^2. Such a division into glancing collisions and close collisions with large momentum transfers is in agreement with Bohr's early semi-classical treatment of stopping [40].

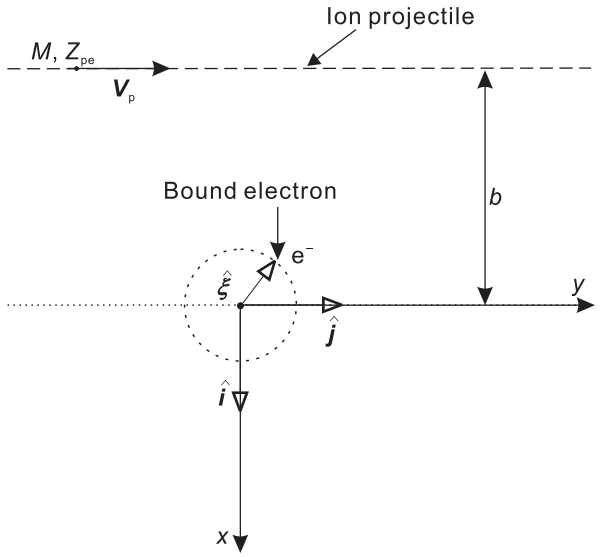

Fig. 16. Schematic of the ion projectile with an extended charge distribution interacting with electrons bound to the partially stripped target. The impact parameter b is assumed larger than the average projectile diameter.

Equation (86) then reads as:

$$\Delta\left(-\frac{\mathrm{d}E}{\mathrm{d}x}\right)_{\omega}=\frac{4\pi n_{\mathrm{T}}Z_{\mathrm{T}}\omega F_{\omega}}{m_{\mathrm{e}}^{2}V_{\mathrm{p}}^{5}}\left(Z_{\mathrm{p}}e^{2}\right)^{3}I\left(\frac{\omega a_\omega}{V_{\mathrm{p}}}\right), \tag{87}$$

where

$$\begin{aligned}I(\xi)\equiv\int_{\xi}^{\infty}\frac{\mathrm{d}u}{u^{2}}\Bigg\{-K_1(u)\int_{-\infty}^{\infty}\mathrm{d}v\,\frac{\cos uv}{(1+v^{2})^{5/2}}\left[\left(v^{2}-2\right)F_1(u,v)\right.\\\left.-3vF_2(u,v)\right]+K_0(u)\int_{-\infty}^{\infty}\mathrm{d}v\,\frac{\sin uv}{(1+v^{2})^{5/2}}\left[3vF_1(u,v)\right.\\\left.-\left(1-2v^{2}\right)F-2(u,v)\right]\Bigg\},\end{aligned} \tag{88}$$

The functions $\boldsymbol{F}_1$ and $\boldsymbol{F}_2$ are defined by

$$F_1(u,v)\equiv\int_{-\infty}^{v}\mathrm{d}y\,\frac{\sin[u(v-y)]}{\left(1+y^{2}\right)^{3/2}},$$

$$F_2(u,v)\equiv\int_{-\infty}^{v}\mathrm{d}y\,\frac{y\sin[u(v-y)]}{\left(1+y^{2}\right)^{3/2}}.$$

K_v is the modified Bessel function of the second kind of order v. For $\xi = \omega a_\omega / V_\mathrm{p} \ll 1$, the function $I(\xi)$ can be approached by $I(\xi) \approx -\frac{3}{2}\pi \ln(\xi) + A$, where $A \approx -2.4$ is a constant. In this case the function $I(\xi)$ vanishes approximately as $I(\xi) \approx \left(\frac{4\pi}{\xi^2}\right)\mathrm{e}^{-2\xi}$.

The fraction $F(\omega)$ of oscillators responding in the frequency range between ω and $\omega + \mathrm{d}\omega$ is given by $g(\omega)\mathrm{d}\omega$, where $g(\omega)$ is the differential oscillator strength normalized such that $\int_0^\infty g(\omega)\mathrm{d}\omega = 1$.

As long as the above result is restricted to large b values $\gg 1$, the corresponding quantum-mechanical derivation would yield to an identical expression (88). Then, the corresponding stopping power correction reads as

$$\Delta\left(-\frac{\mathrm{d}E_\mathrm{p}}{\mathrm{d}x}\right) = \frac{4\pi n_\mathrm{p} Z_\mathrm{T}}{m_\mathrm{e}^2 V_\mathrm{p}^5}\left(Z_\mathrm{p} e^2\right)^3 \int_0^\infty \mathrm{d}\omega g(\omega)\omega\, I\left(\frac{\omega a_\omega}{V_\mathrm{p}}\right). \tag{89}$$

3.1.2. Estimation of equation (88)

The intricate expression (88) may be drastically simplified [41] by invoking an instructive connection with the quadrupole contribution to the electron broadening of neutral lines in Stark broadening theory [43].

Quadratures very similar to

$$M_{\mu,\nu}(z,z') = \int_{-\infty}^{+\infty} \mathrm{d}x\, \frac{\mathrm{e}^{\mathrm{i}zx}}{(1+x^2)^{\mu/2}} \int_{-\infty}^{x} \mathrm{d}y\, \frac{\mathrm{e}^{-\mathrm{i}z'x}}{(1+y^2)^{\nu/2}}$$

have already been reduced to a sum of products of modified Bessel function.

Actually, all the quadratures contributing to $I(\xi)$ may be derived from $M_{\mu,\nu}(z,z')$ and its derivatives with respect to the arguments.

This allows one, after lengthy manipulations, to reduce Eq. (88) to the much simpler expression

$$\frac{I(\xi)}{2\pi} = \xi K_1(\xi)[K_0(\xi)I_0(\xi) - K_1(\xi)I_1(\xi)] + \int_{-\infty}^{\infty} \mathrm{d}u\, K_1(2u)K_1(u)I_1(u), \tag{90}$$

with I_ν as the modified Bessel function of the 1st kind.

- For $\xi \leq 1$, we extend a previous limit with

$$I(\xi) \cong -\frac{3\pi}{2}\ln(\xi) - 2.417 - 2\pi\xi^2\left\{[\ln(\xi)]^2 + 1.14\ln(\xi) - 0.33\right\}, \tag{91}$$

- For large arguments, we get a decay

$$I(\xi) \cong \frac{1}{4}\left(\frac{\pi}{\xi}\right)^{3/2}\mathrm{e}^{2\xi}\xi \to \infty, \tag{92}$$

differing slightly from the Ashley et al. [42,43] expression.

Recalling that $g(\omega)$ is related to the electron distribution $\rho(r)$ in a target atom (ion) by

$$Z_\mathrm{T} g(\omega) = \int \mathrm{d}^3 r \rho(r)\delta[\omega_0(r) - \omega]\,, \qquad \omega_0(r) = \sqrt{\frac{8\pi\rho(r)e^2}{m}} \equiv \sqrt{2\omega_\mathrm{p}} \tag{93}$$

we are now entitled to estimate the Z_p^3 stopping power correction

$$Z_\mathrm{p}^3 J_\mathrm{d} = \frac{4\pi n_\mathrm{T} Z_\mathrm{T}}{m^2 V_\mathrm{p}^5}\left(Z_\mathrm{p} e^2\right)^3 \int_{-\infty}^{\infty} \mathrm{d}\omega(\omega) I\left(\frac{\omega a_\omega}{V_\mathrm{p}}\right) \tag{94}$$

to the enlarged stopping expression

$$\frac{\mathrm{d}E}{\mathrm{d}x} = 2Z_\mathrm{p}^2 I_\mathrm{d} + Z_\mathrm{p}^3 J_\mathrm{d}\,, \tag{95}$$

where the customary lowest-order energy loss (Bohr-Bethe-Bloch) is expressed as twice a long-distance contribution.

Toward that goal we use again the Thomas-Fermi like-GSZ-expression

$$4\pi r^2 \frac{\rho(r)}{N} = \frac{H}{d^2} r \mathrm{e}^{r/d} \frac{H\left(\mathrm{e}^{r/d}+1\right) - 1}{\left[H\left(\mathrm{e}^{r/d}-1\right)+1\right]^3}, \tag{60}$$

Upon introducing a dimensionless ratio $V = V_\mathrm{p}/\sqrt{Z_\mathrm{T}}V_0$ with $V_0 = e^2/\hbar$, the Z_p^2-term becomes

$$I_\mathrm{d} = \frac{C}{\beta^2}\int_0^\infty \mathrm{d}^3 r \rho(r)\xi K_1(\xi)K_0(\xi), \tag{96}$$

with

$$\xi = \sqrt{\frac{\hbar\omega_0(r)}{m_\mathrm{e} r^2}}, \quad C = \frac{4\pi\mathscr{N}_0 e^4}{m_\mathrm{e} c^2} = 0.307\ \left[\mathrm{MeV}\cdot\mathrm{cm}^2\cdot\mathrm{g}^{-1}\right],$$

$\mathscr{N}_0$ being the Avogadro number.

The relative magnitude of the Z_p^3 (Barkas) term is measured finally by:

$$F(V) = \sqrt{Z_\mathrm{T}}V^2\frac{J_\mathrm{d}}{2I_\mathrm{d}}, \tag{97}$$

displayed in Table 5 for four typical atoms and small and large V values respectively. $F(V)$ is typically 15 up to 30 percent of the Z_p^2-term. J_d is obviously a non-negligible quantity. It appears convenient to put Eq. (94) under the form:

$$J_\mathrm{d} = \frac{C}{\beta^2}\frac{2}{\sqrt{Z_\mathrm{T}}}\frac{1}{V}\int \mathrm{d}^3 r \rho(r) I(\xi)\xi^2. \tag{94′}$$

In contradiction to the Lenz-Jensen expression which does not discriminate the atomic structure, GSZ is more selective because it is built upon accurate experimental data for lowest bound states.

Table 5
J_d and $F(V)$ data.

Condition	V	J_d	$F(V)$
	0.5	0.22196	0.327
	1	0.29387	0.371
Ne: $Z = 10$	1.5	0.27711	0.366
$d = 0.427$	9	0.05799	0.179
	9.5	0.05412	0.173
	10	0.05064	0.167
	0.5	0.21793	0.215
	1	0.25206	0.257
Ca: $Z = 20$	1.5	0.23594	0.267
$d = 0.880$	9	0.058472	0.170
	9.5	0.054863	0.166
	10	0.051600	0.162
	0.5	0.20626	0.205
	1	0.24476	0.254
Hg: $Z = 80$	1.5	0.23434	0.271
$d = 0.620$	4	0.14005	0.251
	4.5	0.12717	0.244
	5	0.11601	0.236
	0.5	0.19718	0.178
	1	0.2337	0.231
Th: $Z = 90$	1.5	0.22616	0.252
$d = 0.980$	4	0.13992	0.246
	4.5	0.12757	0.240
	5	0.11678	0.234

3.2. Bloch term

Within the SSM framework outlined in Section 2.2, it is now straight-forward to complete the stopping expression with Barkas $\sim Z_p^3$ and Bloch terms as well. In cold gas, those latter are no longer negligible when the Born parameter $Z_p V_0/(V_p^2 + V_{the}^2)^{1/2}$ is comparable to 1. $V_0 = 1$ in atomic units. V_{th} is the thermal velocity of plasma electrons. Retaining also the very small target-ion contribution, one thus gets a more accurate stopping expression

$$-\frac{dE}{dx} = \frac{4\pi N_0 e^4 \rho Z_p^2}{A_T m_e V_p^2} Z_T \cdot \left[\frac{\overline{Z}}{Z_T} L_0^F + \frac{Z_T - \overline{Z}}{Z_T} L_0^{\overline{B}} + Z_p \frac{V_0}{V_p} + Z_p^2 \frac{V_0^2}{V_p^2} f\left(V_p^2\right) + \frac{m_e}{A_T} Z_T L_p \right], \tag{98}$$

with

$$L_0^F = \ln\left(\frac{2m_e V_p^2}{\hbar\omega_p}\right) - \frac{\langle V_{the}^2\rangle}{V_p^2} - \frac{\langle V_{the}^4\rangle}{2V_p^4} \tag{99}$$

and $\omega_p = \sqrt{4\pi e^2 n_e/m_e}$, the plasma frequency of the target free electrons.

$\langle V_{the}^2\rangle$ is the usual average in terms of Fermi functions. $f(V_p^2)$ accounts for the standard Bloch correction, which bridges a gap between Bohr semi-classical expression and Bethe quantum-mechanical one. The last term $(m_e/A_r)\ Z_T L_p$ accounts for inelastic encounters between ion projectiles and target ions. It is nonnegligible only for $V_p \le V_{the}$, or at a very high plasma temperature.

The third term within brackets in the right-hand side (r.h.s.) of Eq. (98) is the Barkas contribution [44] $\sim Z_p^3$. It pertains only to bound electrons and thus vanishes identically in a fully ionized target. In this case, the Born parameter becomes $Z_p V_0/V_p$.

For $V_p \gg V_{the}$, $L_0^F \to \Lambda_F$ and $L_0^{\overline{B}} \to \Lambda_B$ (cf. Eq. (2)). The relative importance of the four last terms in the rhs of Eq. (98) is evaluated in Table 6 for a target electron density of subsequent experimental interest. Obviously, the Barkas and Bloch corrections to the main Bethe contribution remain rather weak for all values of the Born parameter $Z_p V_0/V_p$.

In the sequel Eq. (98) will be often referred to in the canonical form

$$-\frac{dE}{dx} = k\frac{Z_p^2}{V_p^2}\left[L_0 + Z_p L_1 + f\left(Z_p^2\right)\right]. \tag{100}$$

Bohr, Bethe and Bloch stopping formulae differ essentially from each other in their respective implementation of a classical description combined with the Born approximation. Before attempting a quantitative comparison [39] we consider anew the projectile high velocity expression

$$-\frac{dE}{dx} = \frac{Z_p^2 \omega_p^2 e^2}{V_p^2} L \tag{101}$$

where $\omega_p^2 = 4\pi N_e e^2/m_e$ is the target bulk plasma frequency, with L intrinsically given by Eq. (101) within the selected slowing down expression. To render more transparent the given comparison we consider a fiducial "atom" built on a single harmonically bound electron. It is then easily seen that $I = \hbar\omega$, with ω, electron circular frequency.

So,

$$L_{Bethe} = \ln\left(\frac{2mv^2}{\hbar\omega}\right) - \ln\left(1-\beta^2\right) - \beta^2, \tag{102a}$$

$$L_{Bloch} = \ln\left(\frac{2mv^2}{\hbar\omega}\right) - \frac{1}{2}\ln\left(1-\beta^2\right) - \frac{\beta^2}{2} + \psi(1) - \mathrm{Re}\left[\psi\left(1 + \frac{iZ_p\alpha}{\beta}\right)\right], \tag{102b}$$

$$L_{Bohr} = \ln\left(\frac{1.123mv^3}{|Z_p|e^2\omega}\right) - \ln\left(1-\beta^2\right) - \frac{\beta^2}{2}, \tag{102c}$$

$\psi(x)$ denotes the digamma function, logarithmic derivative of $\Gamma(x)$ and $\alpha = \frac{1}{137.036}$ denotes the fine structure constant.

Relativistic extensions of these expressions feature similarly but are not identical. For instance, half of Bethe relativistic correction arises from distant interactions and one-half stems from close ones. Bohr and Bloch relativistic modifications to distant collisions yield back Bethe's i.e. $-\ln(1-\beta^2) - \beta^2/2$.

Moreover Bethe's relativistic corrections to close interactions apply only within the first Born approximation while similar Bohr and Bloch contributions are not restricted in the same way which leads to a confusing confrontation. Noticing that these relativistic extensions amount only to -7% for $\beta = 0.5$, thus we neglect them in the sequel.

Table 6
Relative importance of Bloch and Barkas terms for cold-gas and plasma target. The target has a linear density of free electron $n_e l = 1.5 \times 10^{19}$ cm^{-2} [D. Gardès, G. Maynard et al., *Phys. Rev.* 146, 5101 (1992)].

		$\frac{Z_p V_0}{V_p}$		Bethe L_0		Barkas		Bloch	
Ion	E (MeV/amu)	Gas	Plasmas	Gas	Plasmas	Gas	Plasmas	Gas	Plasmas
C^{4+}	2	0.56	0.62	5.63	12.48	0.08	0	−0.3	−0.35
S^{7+}	1	1.75	2.07	4.94	11.79	0.35	0	−1.16	−1.32
	1.5	1.43	1.69	5.34	12.2	0.23	0	−0.98	−1.13
	2	1.34	1.47	5.63	12.48	0.18	0	−0.85	−1.00
Br^{6+}	0.93	2.79	3.45	4.86	11.72	0.64	0	−1.61	−1.82

Nonrelativistic expressions for L_{Bethe}, L_{Bloch}, and L_{Bohr} are given on Fig. 17 in terms of as a function of $\ln(\beta)$ at $h\omega = 100$ eV for $Z_p = 1$, 10, and 92. Let us remark that $L_{\text{Bloch}} = L_{\text{Bethe}}$ for $Z_p = 1$ and also that $L_{\text{Bloch}} \sim L_{\text{Bohr}}$ from $\beta \to 0.5$ while $L_{\text{Bloch}} \to L_{\text{Bohr}}$ when $\beta \to 0.05$.

Despite that $L_{\text{Bethe}} = L_{\text{Bohr}}$ at $Z_p = 10$, when $\beta \to 0.13$, both quantities differ by 5% from L_{Bloch}. This highlights a case when a classical result gives back a first-order quantum-mechanical one. Nonetheless both L values turn negative for small β's demonstrating their non-validity for low velocities.

Now it is appropriate to comment on the physics motivating the distinct L behaviors on Fig. 17. Let us first notice that the first Born approximation documents any lowest-order quantum-mechanical one. It is used by Bethe for any kind of collisions while Bloch restricts the use of a first order approximation to distant collisions taken in a dipole approximation. In the non-relativistic case, Bloch considers close interactions with the exact asymptotic's of the Coulomb scattering amplitude altogether with an adequate form of the electron wave packet structure in the c.m. frame allowing a finite and lateral extent of the projectile scattering center in given frame.

Non-relativistic Bloch comes close to non-relativistic Bethe when $|Z_p|\alpha/\beta \leqslant 1 (\geqslant 1)$ from Born (classical) validity. That

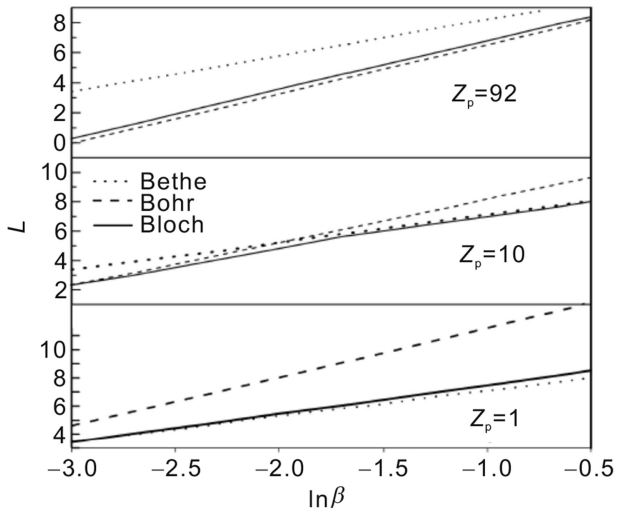

Fig. 17. Nonrelativistic forms of Eqs. (102a), (102b) and (102c). Note that L_{Bethe} is independent of Z_p and that $L_{\text{Bohr}} = L_{\text{Bloch}}$ for $Z_p = 92$, $L_{\text{Bethe}} = L_{\text{Bohr}}$ for $Z_p = 1$ and that $L_{\text{Bloch}} \to L_{\text{Bohr}}$ at small velocities and $L_{\text{Bloch}} \to L_{\text{Bethe}}$ at large velocities for $Z_p = 10$ (after Ref. [39]). Reproduced from S.P. Ahlen, *Rev. Mod. Phys* 52, 121 (1980) with the permission of AIP Publishing.

requirement features the valid approach to close-collision slowing down. It is more difficult to pinpoint distant interactions because the dipole approximation interferes with Born's.

Nonetheless, as Bloch and Bohr use same assumptions for distant collisions while Bloch's treatment retrieves Bohr's even at relativistic energies, any discrepancies between the three approaches should imply close and/or intermediate interactions.

A straightforward contention of this view, due to Bohr, runs as follows: we are allowed to introduce an intermediate impact parameter b_1 so that collisions fulfilling $b > b_1$ can be seen as electromagnetic excitations of charged harmonic oscillators in a homogeneous electric field arising from the passing projectile, while collisions with $b < b_1$ can be seen as free-electron scattering in momentum frame center.

When $b < b_1$, Bohr exact expression is retrieved through $b_1 = Z_p e^2/mv^2\gamma$ with v, relative projectile-electron velocity and $\gamma = (1 - \beta_2) - 1/2$ while restricting to "distant-collision" energy loss.

This is achieved by restricting the impact parameter so that the energy transfer is given as $1/b_2$.

However, when the electron de Broglie wavelength $> Z_p e^2/mv\gamma$ in c.m. frame, it is expected to replace the classical minimum impact parameter which accounts for the elimination of close collisions energy transfer with electron wave packet smearing.

As a result, when $Z_p\alpha/\beta < 1$, quantum-mechanical b_1's lead to Bethe expression while $Z_p\alpha/\beta$ yields back Bohr one. Those conditions feature accurately the validity of first Born and classical approximations, respectively.

3.3. Low velocity stopping

Here, one focuses attention on the slow velocity regime, where the projectile is still transferring a significant amount of energy to the target inner shells. A typical example is afforded by proton beams with initial energy (at pellet entrance) in the MeV range. Then, the range of present concern lies around $E/A \sim 100$ keV, where E denotes the projectile kinetic energy and A, its atomic mass.

Keeping constant effective charge Z_p, present considerations are easily adapted to heavy ion driven fusion, because recent numerical simulations show an enhanced energy transfer between projectiles and target.

To investigate stopping at low velocity, we have to extend the conceptual framework beyond the standard expression (37).

More specifically, it remains to pay a due attention to projectile energy range ($M = Am_p$, m_p being the proton mass)

$$\frac{10^5\,[\mathrm{eV}]}{A} \le \frac{1}{2}MV_p^2 \le 5.15\frac{M}{m_e}Z_T\,[\mathrm{eV}] \tag{103}$$

for which stopping is expected to advocate a frictionlike expression

$$-\frac{dE}{dx} \sim a\left(Z_p e^2\right)^2 V_p \tag{104}$$

with a Brownianlike constant a to be fixed in the sequel. Approximation (104) is fulfilled by RPA free electrons in agreement with $L \sim aV_p^3$ ([1]). Then, the stopping process is viewed as a kind of Brownian motion with the projectile, assaulted by many tiny particles (the stopping electrons). Up to now, we advocated a $Z_p \ll Z_T$ regime, which is to be contrasted to the case $Z_p \cong Z_T$ considered in the literature (e.g. for instance the so-called LSS model [45,46] through a quasi-molecular approach.

Eq. (104) may be derived in the impulse approximation (IA) when the Born validity criterion,

$$\frac{Z_p e^2}{\hbar V_0} \ll 1. \tag{105}$$

$V_0 =$ average bound target electron velocity, is fulfilled (by close collisions, for instance). Then, the stopping contribution of bound subshell $I(\equiv n, l)$ is explained as

$$-\frac{1}{4\pi n_T}\left(\frac{dE}{dx}\right)_{nl} = \frac{\left(Z_p e^2\right)^2}{m_e V_p^2}\int_0^\infty dE' \int_{\frac{E}{\hbar V_p}}^\infty \frac{dq}{q}\frac{df_{nl}(q,E')}{dE'} \tag{106}$$

in terms of the generalized oscillator strength (GOS) density $\frac{df_{nl}}{dE}$ labelled by excitation energies E and the impulse $\hbar q$ transferred from projectile to target electron. n_T.

Within the impulse approximation (IA), df_n/dE is expressed in terms of the p-space target wave functions $\chi_{nl}(p)$, retaining their unperturbed labelling (n, l). After several transformation, Eq. (106) may be given the form (104), with

$$a = \frac{m_e}{3E_I}\left\langle\frac{1}{p}\right\rangle_{nl} \tag{107}$$

showing that, the best accuracy can be expected for eigen-quantities of the stopping electron. However, the most serious drawback is the insufficiently accurate E_I for the highest subshells which provide the largest stopping. Generally speaking, weakly bound electrons seem more efficient stoppers than more tightly bound ones. The IA results compare pretty well (Fig. 18) with the Andersen-Ziegler compilation [47] for low velocity stopping of protons in cold argon gas.

The extrapolations from Bethe formula stand down by more than a factor of 2.

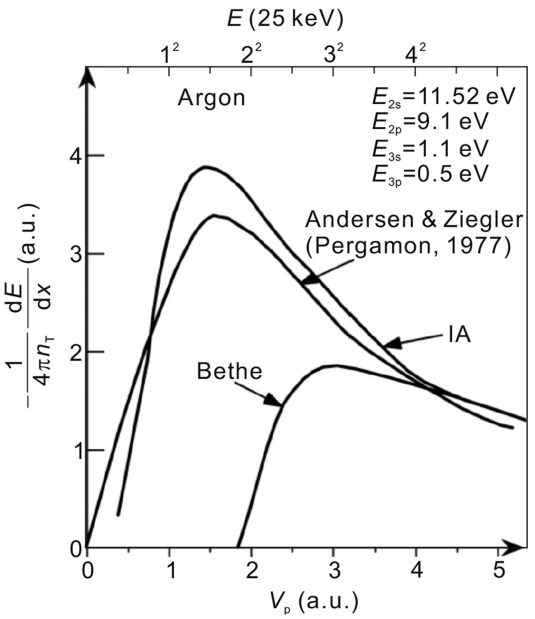

Fig. 18. Impulse approximation (IA) results compared with experimental values and Bethe formula for stopping by neutral argon. Pergamon refers to Ref. [47].

4. Low velocity ion stopping in binary ionic mixtures (BIM) [48]

A specific interest devoted to low velocity ion slowing down (LVISD) in dense multicomponent plasmas has recently emerged in conjunction with a few other topics featuring concerns for inertially confined fusion (ICF) operated through super intense and femtosecond laser produced ion beams. As expected, this trend got initiated with the routine production of proton beams with a kinetic energy up to 100 MeV and also highlighting a very small transverse emittance. An intense activity is thus presently deployed to extending the proton performances up to fully ionized carbon ions (C^{6+}) and heavier ions whenever possible. Moreover, the quantitative control of the standard fusion reaction based on the deuterium-tritium (DT) fuel sustained by the resulting α particles (He^{2+}) requires a thorough investigation of an α LVSID near the end of range.

This explains that we pay a certain attention to proton and α stopping in dense DT-mixtures with a variable relative composition with density range $10^{23} < n_e\,[\mathrm{cm}^{-3}] < 10^{26}$ and thermal velocity range $10 < T\,[\mathrm{eV}] < 20\,000$. An adequate and fine tuning out of the relevant LVISD is thus expected for the beam-target interaction involved in the fast ignition scenario (FIS).

It is also worthwhile to mention the strong relevance of LVISD to many astrophysics issues, and also in the production through heavy ion beams stopped near Bragg peak in thin targets, of the so-called warm dense matter (WDM) i.e strongly coupled plasmas with a density close to the solid one and a few eV temperature [49].

4.1. Basic formulation

Basically, LVISD features canonically as

$$-\frac{\mathrm{d}E}{\mathrm{d}x} = AV_\mathrm{p}, \tag{108}$$

for a typical energy/nucleon <100 keV/nucleon.

The pertaining dielectronic picture includes partially degenerate electrons and classical ion species (Z_i, M_i) as well. The ion component highlights a weakly coupled BIM. Then, it appears appropriate to introduce the overall dielectronic function

$$\varepsilon(\boldsymbol{k},\omega) = 1 + \frac{1}{k^2}\left[W\left(\frac{W}{k}\right) + W\left(\sqrt{M_1}\,\frac{W}{k}\right) + W\left(\sqrt{M_2}\,\frac{W}{k}\right)\right] \tag{109}$$

with the usual Fried-Conte dispersion function W (Im $\zeta \geq 0$)

$$W(\zeta) = \frac{1}{\sqrt{2\pi}}\lim_{\nu\to 0+}\int_{-\infty}^{\infty}\mathrm{d}x\frac{x\mathrm{e}^{-x^2/2}}{x-\zeta-\mathrm{i}\nu} \tag{110}$$

and $X(\zeta) = \mathrm{Re}W(\zeta), \quad Y(\zeta) = \mathrm{Im}W(\zeta)$.

Extending the standard one-component stopping expression

$$-\left(\frac{\mathrm{d}E}{\mathrm{d}x}\right) = \frac{Z^2N_\mathrm{D}}{(2\pi)^2}\int_{\infty}^{k}\mathrm{d}k\cdot k^3\int_{-1}^{+1}\mathrm{d}\mu\frac{\mu Y(\mu V_\mathrm{p})}{\left[k^2+X(\mu V_\mathrm{p})\right]^2+Y^2(\mu V_\mathrm{p})} \tag{111}$$

with $Z = Z_\mathrm{eff}/N_\mathrm{D}$, where Z_eff denotes the projectile effective charge at velocity V_p, $N_\mathrm{D} = n_\mathrm{e}\lambda_\mathrm{D}^3$ in terms of target electron density and corresponding Debye length. In the sequel, V_p will be scaled by $V_\mathrm{the} = \sqrt{k_\mathrm{B}T/m_\mathrm{e}}$, thermal electron velocity with T, thermalized target temperature. In Eq. (111) we select k_max by considering quantum diffraction effects when $k_\mathrm{B}T \geqslant 1\mathrm{Ry}$ so that

$$\begin{aligned} k_\mathrm{max} &= \min\left[\frac{m\left(V_\mathrm{p}^2+V_\mathrm{the}^2\right)}{Z_\mathrm{eff}}, \frac{2m\sqrt{V_\mathrm{p}^2+V_\mathrm{the}^2}}{\hbar}\right] \\ &= \min\left[\frac{4\pi}{Z}\left(V_\mathrm{p}^2+2\right), 8\pi\sqrt{2N_\mathrm{D}}\,\frac{\alpha c}{V_\mathrm{the}}\sqrt{V_\mathrm{p}^2+2}\right], \end{aligned} \tag{112}$$

where V_p is now dimensionless on the second line on the right-hand-side, $\alpha = 1/137.036$ is the fine structure constant, and c, light velocity.

The specification of Eq. (111) to BIM stopping requires the relative ion concentration of species 1, i.e.

$$\alpha = \frac{N_1}{N_1+N_2} \tag{113}$$

in terms of ion number N_i with $i = 1, 2$, in target plasma, so that BIM densities

$$n_1 = \frac{n_\mathrm{e}\alpha}{\overline{Z}}, \quad n_2 = \frac{n_\mathrm{e}(1-\alpha)}{\overline{Z}}, \quad \overline{Z} = Z_1\alpha + Z_2(1-\alpha) \tag{114}$$

are straightforwardly expressed in terms of electron density n_e.

Then, we can estimate the stopping contributions of every target component: electron 0, ion 1 and ion 2 as follows:

$$\frac{\mathrm{d}E_0}{\mathrm{d}x} = C_0\int_0^{K_{\mathrm{max}_0}}\mathrm{d}k\cdot k^3\int_{-1}^{+1}\mathrm{d}\mu\frac{\mu Y(\mu v)}{D(k,\mu v)}, \tag{115a}$$

$$\frac{\mathrm{d}E_1}{\mathrm{d}x} = C_1\int_0^{k_{\mathrm{max}_1}}\mathrm{d}k\cdot k^3\int_{-1}^{+1}\mathrm{d}\mu\frac{\mu Y(\sqrt{M_1}\mu v)}{D(K,\mu v)}, \tag{115b}$$

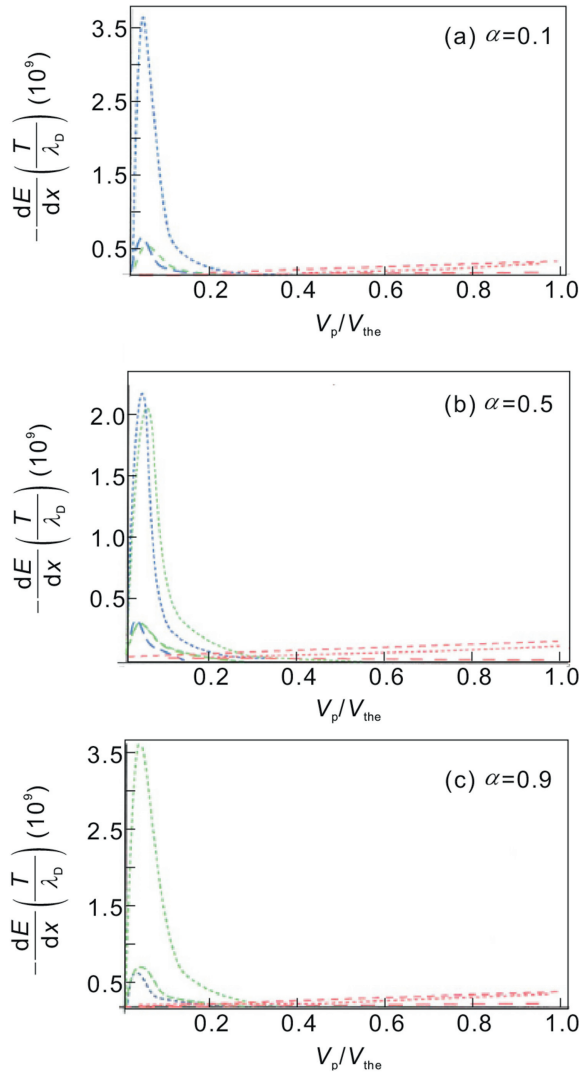

Fig. 19. Proton stopping in H^+–D^+ BIM in terms of $V_\mathrm{p}/V_\mathrm{the}$•$n_\mathrm{e} = 10^{23}$ cm^{-3}, α denotes the proton concentration in BIM T = … 10 eV, – – 100 eV, — — 1000 eV. Red pertains to e-stopping, green to H^+-stopping and blue to D^+-stopping. Reproduced from B. Tashev, et al., *Phys. Plasmas* 15, 102701 (2008) with the permission of AIP Publishing.

$$\frac{\mathrm{d}E_2}{\mathrm{d}x} = C_2 \int_0^{k_{\max_2}} \mathrm{d}k \cdot k^3 \int_{-1}^{+1} \mathrm{d}\mu \frac{\mu Y(\sqrt{M_2}\mu v)}{D(K,\mu v)}, \tag{115c}$$

where

$$D(k,\mu v) = \left[k^2 + X(\mu v) + X\left(\sqrt{M_1}\mu v\right) + X\left(\sqrt{M_2}\,\mu v\right)\right]^2 + \left[Y(\mu v) + Y\left(\sqrt{M_1}\mu v\right) + Y\left(\sqrt{M_2}\,\mu v\right)\right]^2, \tag{116}$$

and

$$C_0 = \frac{k_\mathrm{B} T Z_\mathrm{eff}^2}{4\pi^2 n_\mathrm{e} \lambda_\mathrm{D}^4},$$

$$C_1 = \frac{C_0 Z_1^4 \alpha}{\overline{Z}},$$

$$C_2 = \frac{C_0 Z_2^4 (1-\alpha)}{\overline{Z}},$$

altogether with

$$k_{\max_0} = \mathrm{Min}\left[k_{\max_0^1} = n_\mathrm{e}\lambda_\mathrm{D}^3 \frac{4\pi(v^2+2)}{Z_\mathrm{eff}}, \; 14.78 n_\mathrm{e}\lambda_\mathrm{D}^3 \sqrt{\frac{v^2+2}{k_\mathrm{B}T}}\right], \tag{117a}$$

$$k_{\max_1} = \frac{k_{\max_0^1}}{Z_1^3}\left(\frac{\overline{Z}}{\alpha}\right)^{1/2}, \tag{117b}$$

$$k_{\max_2} = \frac{k_{\max_0^1}}{Z_2^3}\left(\frac{\overline{Z}}{1-\alpha}\right)^{1/2}, \tag{117c}$$

Expressions (115) are in $k_\mathrm{B}T/\lambda_\mathrm{D}$, with the Debye screening length λ_D respectively adapted to electron 0, ion 1 and ion 2. V_p is in V_the.

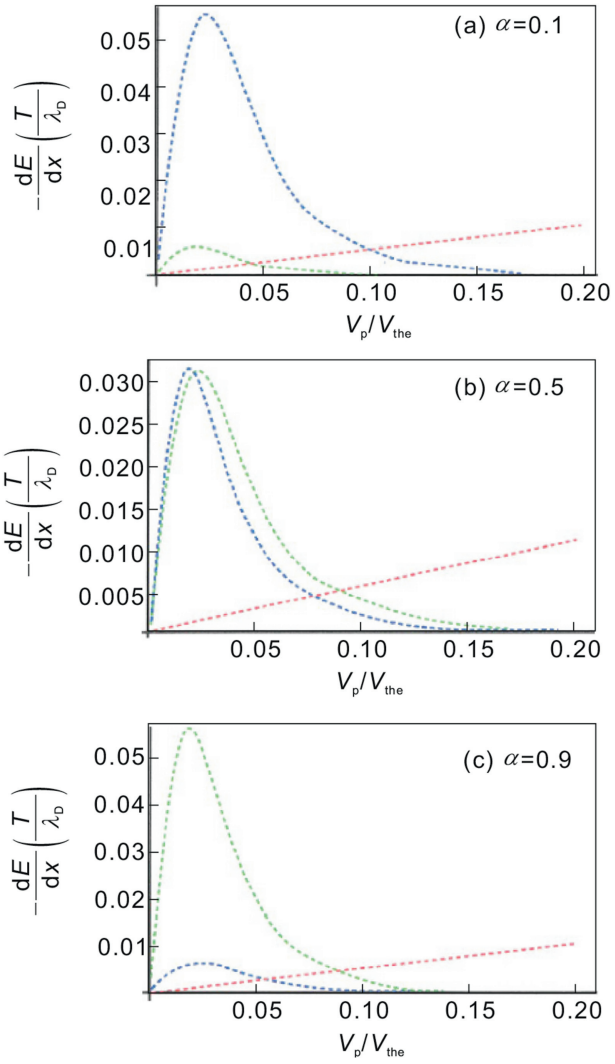

Fig. 20. Alpha particle stopping in a Tokamak-like D-T BIM with $n_\mathrm{e} = 10^{14}$ cm^{-3} and $T = 10$ keV. α denotes D^+-concentration. Red refers to e-stopping, green to D^+-stopping and blue to T^+-stopping. Reproduced from B. Tashev et al., *Phys. Plasmas* 15, 102701 (2008) with the permission of AIP Publishing.

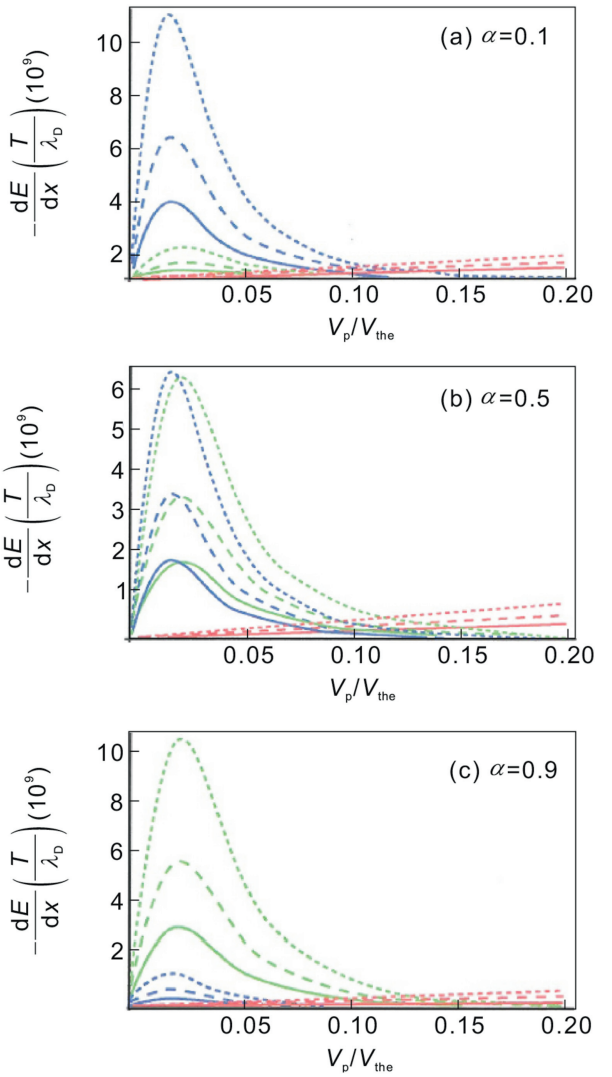

Fig. 21. Proton stopping in a DT-mixture. $n_\mathrm{e} = 10^{25}$ cm^{-3}, $T =$ … 0.5 keV, – – 1 keV, — — 2 keV. Red refers to e-stopping, green to D^+-stopping and blue to T^+-stopping. Reproduced from B. Tashev et al., *Phys. Plasmas* 15, 102701 (2008) with the permission of AIP Publishing.

4.2. Main stopping trends

4.2.1. Basic feature

We detail now the LVISD specificities in the DT-BIM in the velocity range $V_{thi} < V_p < V_{the}$. Stressing the usual target parameters, density, temperature, and the charge and mass (M_i, Z_i) of ion species i, we notice that a pertinent bookkeeping of stopping modes has to be performed for a projectile stopping power measured in $k_B T/\lambda_D$, in terms of the target equilibrium temperature T and screening Debye length λ_D, respectively, featuring the electron contribution (e-stopping) and the ion contribution $i = 1, 2$. Moreover, we shall frequently reduce the projectile effective charge Z_{eff} to that of the proton, because the k_{max} [Eq. (117)] Z_{eff} dependence remains very weak, so the usual quadratic dependence Z_{eff}^2 of the stopping patterns shows up as fulfilled in the whole space parameter of present interest.

We first focus on deuterium-tritium (DT) BIM of thermonuclear fusion interest, with a strong emphasis on superdense DT target considered for the so-called fast ignition scenario (FIS) in inertial fusion energy (IFE).

Stressing the stopping of the thermonuclear produced α particles, we remark that as soon as the target temperature T lies above 1 keV, the corresponding α particles velocity V_p should remain below the target thermal electron velocity V_{the}. So the crucial self-sustained target ignition through He^{2+} stopping in DT-targets is strongly dependent on LVISD mechanisms considered here.

On the other hand, proton stopping remains a major issue for assessing the feasibility of FIS/IFE in view of the recently advocated potential of very intense proton beams produced in the irradiation of thin solid foils by PW-lasers. The given proton beams show a very low transverse emittance, which are easier to handle than the relativistic electron beams (REB) initially selected out.

The very fine tuning of the tiny hot spots produced in the bombardment of DT targets, demands that the proton end of range be carefully monitored through LVISD.

Denoting α as the relative proportion of ion species A in the so-called AB-BIM and expliciting in Fig. 19 the α-dependence of the stopping profiles (SP) in terms of dimensionless projectile velocity $0 \leqslant V_p/V_{the} \leqslant 1$, for proton projectiles losing their energy in a $H^+ - D^+$ BIM at solid density $n_e = 10^{23}$ cm^{-3} and $T = 10-1000$ eV, BIM stopping appears essentially restricted to the narrow range $0 \leqslant V_p/V_{the} \leqslant 0.2$.

Blue qualifies projectile stopping through the D^+-ionic component, green pertains to the target H^+-component, and red highlights the usual e-stopping treated classically in view of $T \geqslant 10$ eV $> T_F = 7.85$ eV. In this V_p range, e-stopping remains secondary to i-stopping.

Lower T-values would emphasize $\hbar \neq 0$ effects due to electron partial degeneracy through T-dependent electron-ion and electron-electron effective interactions.

The code of colors runs as follows: Black for blue lines, dark gray for red lines, and light gray for green lines. The most conspicuous feature highlighted by the α-dependence of Fig. 19 is obviously the quasi symmetry $\alpha \Leftrightarrow 1 - \alpha$ due to $Z_1 = Z_2$ and $M_2/M_1 = 1.5$.

Such a behavior is also fulfilled by a D-T BIM exposed to a He^{2+} beam at a much lower density $n_e = 10^{14}$ cm^{-3}, qualifying an MFE-like plasma at $T = 10$ keV. The given quasi symmetry is also updated in both situations by the nearly equal ion stopping contributions at $\alpha = 0.5$.

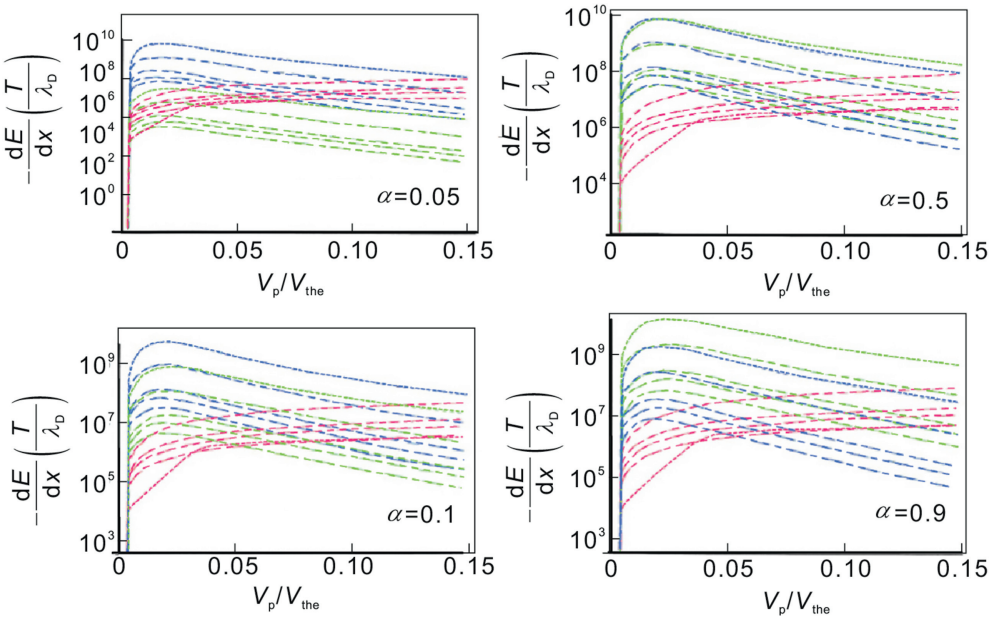

Fig. 22. Alpha particle projectile in a Deuterium-Tritium BIM with $n_e = 10^{23}$ cm^{-3} and different temperatures with D^+ relative proportion. (a) $\alpha = 0.001$, (b) $\alpha = 0.1$, (c) $\alpha = 0.5$ and (d) $\alpha = 0.9$. Red refers to electron stopping, green to D^+-stopping while blue denotes T^+-stopping; Dots refer to $T = 10$ eV, other lines with the same color denote $T = 100$ eV, 2 keV and 5 keV from top to bottom. Reproduced from B. Tashev, et al., *Phys. Plasmas* 15, 102701 (2008) with the permission of AIP Publishing.

Let us remark that the sum of the highest ordinates of the ion SP keeps a value constant when α varies, at fixed temperature. All those trends are shared by proton stopping in a superdense mixture (Fig. 22 of FIS concern with $n_e = 10^{25}$ cm^{-3} and $T = 0.5 - 2$ keV. It is also a remarkable fact that target ion SP peaks always appear at very low $V_p/V_{the} < 0.05$, in the three cases (Figs. 19 and 22) herein considered.

4.2.2. T-dependence

FIS ignition performances strongly rely on the the compressed DT-fuel initial temperature. In this regard we show on Figs. 23 and 24 the stopping profiles (SP) on a logarithmic scale for alpha particle slowing down at 10^{23} cm^{-3} and 10^{26} cm^{-3}, respectively.

With this change of scale, the e-stopping does not appear negligible and fine structures at the intersection of e-stopping and i-stopping are clearly seen, α denotes deuterium relative concentration and the quasi-symmetric features of target ions SP look even enhanced contrasted to their linear counterparts.

4.2.3. Critical velocity $V_{p,crit}$

Above displayed stopping data make it clear that target e-stopping contribution matches the sum of remaining i-projectile stopping contributions for a critical projectile velocity $V_{p,crit}$ such that $V_{p,crit}/V_{the} \sim 0.15 - 0.2$, when the given BIM are not too asymmetric in charge and mass.

This process is illustrated in Fig. 24 through proton stopping down in a $H^+ - He^{2+}$ BIM with $10^{12} \leqslant n_e\ [cm^{-3}] \leqslant 10^{18}$ and $0 \leqslant T\ [eV] \leqslant 10^3$. Fig. 24(a) highlights a rather flat three-dimensional snapshot for a $\alpha = 0.5$ BIM vindicating $0.1 \leqslant V_{p,crit}/V_{the} \leqslant 0.13$. However, separate variations in T [Fig. 24(b)] and density [Fig. 24(c)] document a strong α-dependence for $V_{p,crit}$. It is a remarkable fact that these $V_{p,crit}$ estimates fall in quite a close agreement with those derived from an independent Fokker-Planck analysis, relying on the ratio of projectile kinetic energy to that of target electrons.

Thus we get

$$\frac{\frac{1}{2}M_p V_{p,crit}^2}{\frac{1}{2}m_e V_{the}^2} = \frac{C^{2/3}}{\frac{1}{2}m_e V_{the}^2} \tag{118}$$

where

$$C = \frac{3\pi^{1/2}}{4}\left(\frac{M_p}{m_e}\right)^{1/2}\frac{M_p}{\overline{M}}\overline{Z}$$

in terms of the BIM quantities $\overline{Z} = \alpha Z_1 + (1-\alpha)Z_2$ and $\overline{M} = \alpha M_1 + (1-\alpha)M_2$. In the present case, the above ratio becomes

$$\frac{V_{p,crit}}{V_{the}} \cong 0.12$$

in rather good agreement to that displayed on the Fig. 24(a) vertical scale. A similar quantitative matching between the present dielectric approach and the collisional one of current use in Tokamak physics can be retrieved for alpha particle stopping, as well.

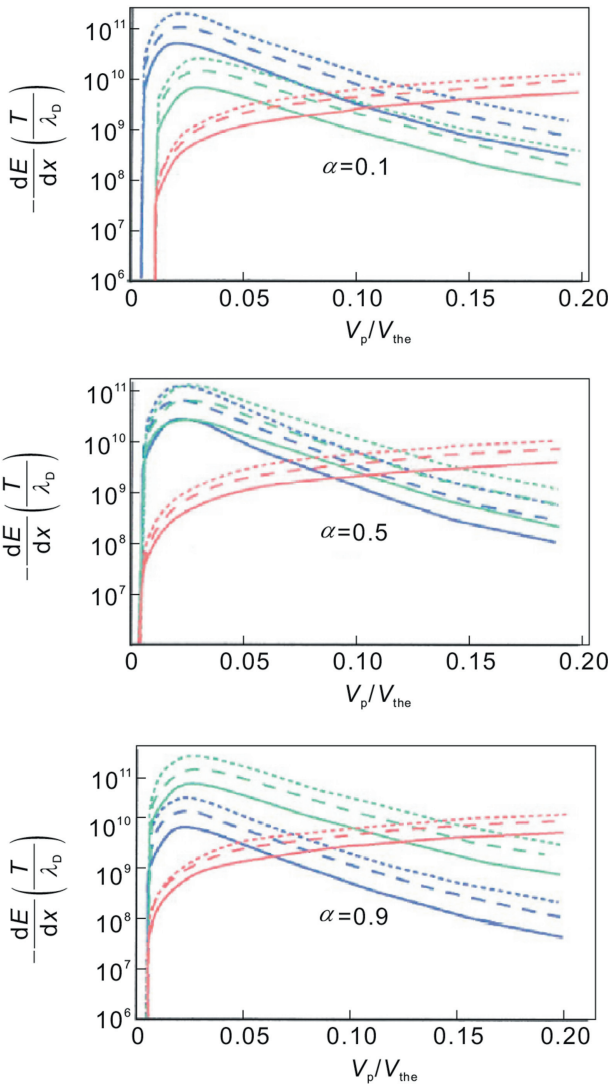

Fig. 23. He^{2+} projectile in a deuterium-tritium mixture where $n_e = 10^{26}$ cm^{-3} and $T =$ … 1 keV, – – 2 keV, — — 5 keV with α deuterium relative concentration. Color attribution are the same as in Fig. 22. Reproduced from B. Tashev et al., *Phys. Plasmas* 15, 102701 (2008) with the permission of AIP Publishing.

4.2.4. Straggling

Within the rather high temperature range of present interest, one can use the high-T straggling approximation,

$$\Omega^2 = 2k_B TS \tag{119}$$

where S is the total stopping including electron and ion contributions. Fig. 25 illustrates the case of proton projectiles stopped in a DT-equimixture ($\alpha = 0.5$) with $n_e = 10^{18}$ cm^{-3} and $T = 500$ eV. It unambiguously contrasts the usual bell-shaped curve featuring e-stopping at any V_p, to the highly peaked BIM contribution restricted to $V_p/V_{the} \leq 0.2$.

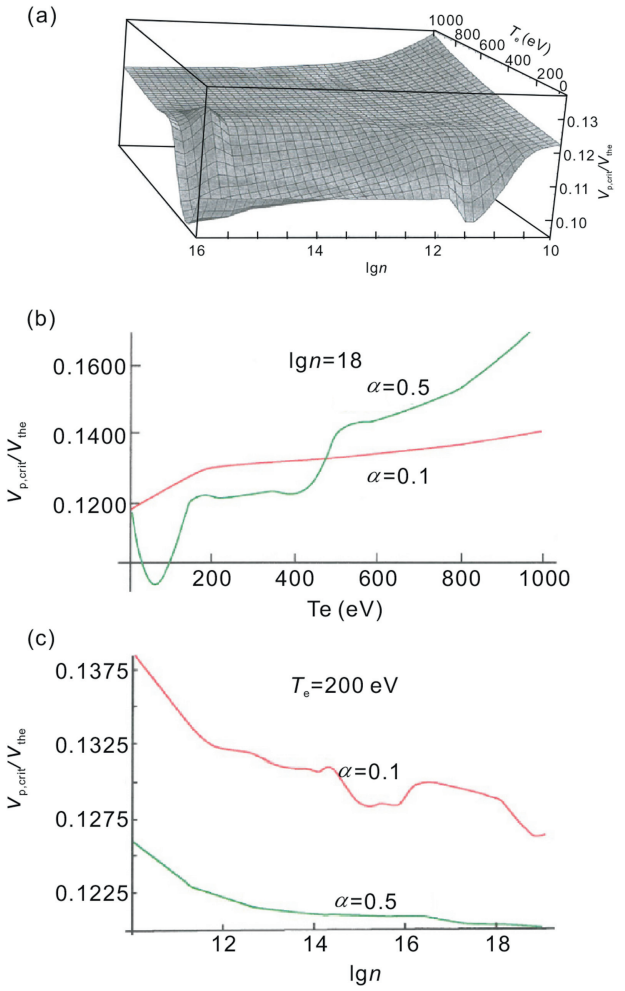

Fig. 24. Critical proton velocity $V_{p,crit}$ in $\alpha = 0.5$ H^+–He^{2+} BIM. (a) 3D view in terms of n_e and T, (b) cross-section at $n_e = 10^{18}$ cm^{-3} for $\alpha = 0$ and 0.5, (c) cross-section at $T = 200$ eV for $\alpha = 0.1$ and 0.5. Reproduced from B. Tashev et al., *Phys. Plasmas* 15, 102701 (2008) with the permission of AIP Publishing.

5. Conclusion and outlook

The present review of ion stopping in dense plasmas appears mostly geared toward theoretical and simulation features. However, corresponding experimental aspects already previously referred to [2] demand also a timely updating motivated by very recent and significantly promising developments.

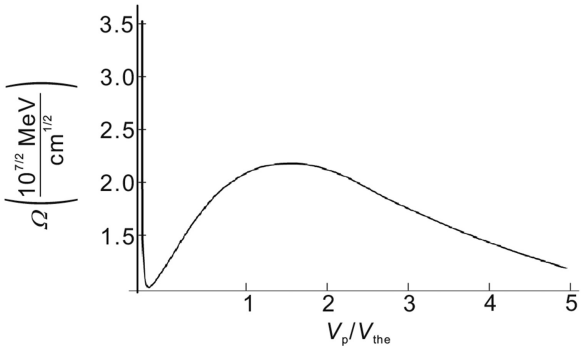

Fig. 25. High temperature straggling for proton projectiles in a DT-BIM with $\alpha = 0.5$, $n_e = 10^{18}$ cm^{-3} and $T = 500$ eV. Reproduced from B. Tashev et al., *Phys. Plasmas* 15, 102701 (2008) with the permission of AIP Publishing.

In this regard, the potentialities afforded by intense ion beams to emulate high energy density physics have just been presented by Sharkov et al. [54] which details, for instance, the specific ion-plasma target designs such as HIHEX and PRIOR envisioned for isochoric plasma heating and proton radiography.

Pertaining facilities include FAIR at GSI – Darmstadt (presently in construction) as well the HIAF combination in China headed by IMP-Lanzhou.

Typically, these setups would secure intense and highly charged ($Z \sim 33$) uranium beams with up to 4.4×10^9 particles/bunch in 100–125 ns.

Then, the given and possible beam–target configurations appear very well suited to document heating of warm dense matter (WDM) plasmas with $T \sim 1 - 10$ eV in a volume $\sim$ mm^3 much larger than the biggest ones affordable on the most performing laser beam lines (LCLS at SLAC for instance) while featuring only small density gradients at plasma edges.

Specific energy deposit is thus expected up to 100 MJ/g enabling the investigation of hot plasma targets with T up to 1 keV.

Other significant highlights concern the very first and accurate determination of light ion (proton and α particle) stopping in the vicinity of the Bragg peak ($V_p \sim V_{the}$) by Frenje et al. [55] using SiO_2 thin capsules filled with D-^{3}HeHe gas in same proportion. Strength and location of the Bragg peak are demonstrated strongly dependent on density (~10^{23} cm^{-3}) and temperature ($T \sim 0.4 - 0.5$ keV) variations in plasmas of current inertial fusion interest.

The same MIT-LLE team headed by Petrasso [56] in collaboration with others also carefully investigated proton stopping in WDM targets with $T \sim 32$ eV at moderate Coulomb coupling (0.3) and moderate electron degeneracy ($T/T_F \sim 2$).

In this regard, it is worthwhile to notice that such investigations open the door to a systematic inquiry of nonrelativistic ion stopping in arbitrary degenerate electron targets [1,57]. Moreover, an intriguing and promising possibility for measuring stopping and straggling of very light ions such as protons and α particles got very recently implemented [58] through the simultaneous use of the same high power laser to ignite a target plasma in a gas jet and also to produce the interacting ion beam out of the usual TNSA (target normal sheath acceleration) mechanism.

For that purpose, two arms on the setups ELFIE (Ecole Polytechnique) and TITAN (Lawrence Livermore) have been respectively selected to produce a short TNSA pulse (10 J, 400 fs) and a long pulse (60 J, 500 ps). The latter one being devided in two-halves enabling target firing and also a probing beam (~30 mJ, 400 fs).

This novel metrological approach could allow to probe very conveniently different target plasmas (H, He, N, Ar, Xe …) at high temperature ($100 < T_e$ [eV] < 1000) with a target density $n_e \sim 10^{20}$ cm^{-3} while using a well energy–calibrated impacting ion beam through a carefully designed velocity

selector out of the initially and laser produced broadband beam. Then, the corresponding ion-plasma interactions stand at variance to the former accelerator-based ones [2,3,50-53] restricted to moderate temperatures ($1 < T_e\,[\mathrm{eV}] < 10$) [2,3].

References

[1] C. Deutsch, G. Maynard, Stopping of pointlike charges in a dense electron fluid, Recent Res. Devel. Palsmas 1 (2000) 1−23.

[2] C. Deutsch, G. Maynard, M. Chabot, D. Gardes, S. Della-Negra, et al., Ion Stopping in dense plasma target for high energy density physics, Open Plasma Phys. J. 3 (2010) 88−115.

[3] R.O. Bangerter, Targets for heavy ion fusion, Fus. Technol. 13 (1988) 348−355;
Ion beam interaction with ICF targets, Las. Int. Rel. Plasma Phen. 6 (1984) 1013−1027.

[4] H.D. Betz, Ion projectile effective charge in, Appl. At. Coll. Phys. 4 (1984) 1−42.

[5] D.S. Bailey, Y.T. Lee, R.M. More, Ab initio calculations of the charge state of a fast heavy ion stopping in a finite temperature target, J. Phys. (Paris) 44 (C8) (1983) 149−158.

[6] E. Nardi, Z. Zinamon, Charge state and slowing of fast in plasmas, Phys. Rev. Lett. 49 (1982) 1251−1254;
G. Maynard, C. Deutsch, Interaction of heavy ions with gas and plasma targets, J. Phys. (Paris) 49 (C7) (1988) 89−97.

[7] G.I. Bell, The capture and loss of electrons by fission fragments, Phys. Rev. 90 (1953) 548−557.

[8] Th. Peter, J. Meyer-Ter-Vehn, Energy loss of heavy ions in dense plasma. II Nonequilibrium charge states and stopping powers, Phys. Rev. A 43 (1991) 2015−2030.

[9] M. Gryzinski, Two-particle collisions. I. General relations for collisions in the laboratory system, Phys. Rev. 138, A (1965) 305−321;
M. Gryzinski, Two-particle collisions. II. Coulomb collisions in the laboratory system of coordinates, Phys. Rev. 138, A (1965) 322−325;
J.H. McGuire, P. Richard, Procedure for computing cross sections for single and multiple ionization of atoms in the binary-encounter approximation by the impact of heavy particles, Phys. Rev. A8 (1973) 1374−1384.

[10] W. Lotz, An empirical formula for the electron-impact ionization cross-section, Zeitschrift für Physik A Hadrons and Nuclei 206 (1967) 205−211.

[11] Ya. B. Zel'Dovich, Yu.P. Raizer, Physics of Shock Waves and High-Temperature Hydrodynamic Phenomena vol. 1, Academic Press, New-York, 1966, p. 406.

[12] D.H. Menzel, The physical processes in gaseous nebulae 1. Absorption and emission radiation, Astrophys. J. 85 (1937) 330−339;
L. Spitzer, The temperature of interstellar matter 1., Astrophys. J. 107 (1948) 6−33.

[13] J.R. Oppenheimer, On the quantum theory of the capture of electrons, Phys. Rev. 31 (1928) 349−356;
H.C. Brinkman, H.A. Kramers, The theory of the collection of electrons by means of α-particles, Proc. Ned. Akad. Wet. 33 (1930) 973−984.

[14] G. Maynard, W. Andre, M. Chabot, C. Deutsch, C. Fleurier, et al., Charge evolution of swift heavy ions in fusion plasmas, Nuo. Cim. 106A (1993) 1825−1993.

[15] Th. Peter, R. Arnold, J. Meyer-Ter-Vehn, Influence of dielectronic recombination on fast ion charge states in a plasma, Phys. Rev. Lett. 57 (1986) 1859−1862.

[16] V.L. Jacobs, J. Davis, P.C. Kepple, P. Blaha, The influence of auto-ionization accompanied by excitation on dielectronic recombination and ionization equilibrium, Astrophys. J. 211 (1977) 605−616.

[17] G. Maynard, C. Deutsch, Dynamical effect and dielectronic recombination of fast heavy ions in a plasma, Phys. Scr. 48 (1993) 471−473.

[18] G. Maynard, C. Deutsch, P. Fromy, K. Katsonis, Atomic physics for inertial fusion using average correlated hydrogenic atom model, Laser Part. Beams 13 (1995) 271−279.

[19] H.D. Betz, L. Grodzins, Charge states and excitation of fast heavy ions passing trhough solids : A new model for the density effect, Phys. Rev. Lett. 25 (1970) 211−214.

[20] C. Couillaud, R. Deicas, Ph. Nardin, M.A. Beuve, J.M. Guihaume, et al., Ionization and stopping of heavy ions in dense laser-ablated plasmas, Phys. Rev. E49 (1994) 1545−1562.

[21] M.H. Chen, Relativistic intermediate-coupling calculations of dielectronic-recombination coefficients for the Li isoelectronic sequence, Phys. Rev. A44 (1991) 4215−4223.

[22] Th Peter, R. Arnold, J. Meyer-Ter-Vehn, Private Communication, 1985.

[23] C.L. Pekeris, 11S and 23S states of helium, Phys. Rev. 115 (1959) 1216−1221.

[24] A. Dalgarno, The stopping powers of atoms,, Proc. Phys. Soc. 76 (1960) 422.

[25] U. Fano, J.W. Cooper, Spectral distribution of atomic oscillator strengths, Rev. Mod. 40 (1968) 441−507;
I. Shimamura, T. Watanabe, Bounds on mean excitation energies in terms of oscillator-strength moments, Phys. Rev. A 23 (1981) 2914−2915.

[26] I. Shimamura, T. Watanabe, Bounds on mean excitation Energies, lamb-shift, stopping power, straggling and grazzing collision of high charged particles, J. Phys. Soc. Jap. 34 (1973) 483.

[27] J.L. Dehmer, M. Inokuti, R.P. Saxon, Systematics of moments of dipole oscillator-strength distributions for atoms of the first and second rows, Phys. Rev. A12 (1975) 102−121.

[28] A.E.S. Green, D.L. Sellin, A.S. Zachor, Analytic independent-particle model for atoms, Phys. Rev. 184 (1969) 1−9;
R. Garvey, C.H. Jackman, A.E.S. Green, Independent-particle model potentials for atoms and ions with $36<Z\leq54$ and a modified Thomas-Fermi atomic energy formula, Phys. Rev. A12 (1975) 1144−1152.

[29] X. Garbet, C. Deutsch, G. Maynard, Mean excitation energies for ions in gases and plasmas, J. Appl. Phys. 61 (1987) 907−916.

[30] J.H. Peek, L.C. Pitchford, E.J. Shipsey, Methods for predicting stopping and straggling mean excitation energies, Phys. Rev. A29 (1984) 1096−1102.

[31] J. Bell, D.R.B. Bish, P.E. Gill, Separate subshell contribution to the stopping power of rare gases, J. Phys. B5 (1972) 476−482.

[32] B.F. Rozsnayi, Relativistic Hartree-Fock-Slater calculations for arbitrary temperature and matter density, Phys. Rev. A5 (1972) 1137−1149.

[33] D.A. Liberman, D.T. Cromes, J.T. Waber, Average atom models in dense plasmas, Compt. Phys. Comm. 2 (1971) 107.

[34] J. Lindhard, M. Scharff, Energy loss in matter by fast particles of low charge, Dan. Vidensk. Selsk. Math. Fys. Medd. 27 (15) (1953) 1−31.

[35] R.E. Johnson, M. Inokuti, The local plasma approximation to the oscillation strength spectrum: How good is it and why? Comm. At. Mol. Phys. 14 (1983) 19−31.

[36] T.A. Mehlhorn, A finite material temperature model for ion energy deposition in ion-driven inertial confinement fusion targets, J. Appl. Phys. 52 (1981) 65226532.

[37] C. Deutsch, G. Maynard, H. Minoo, Ion stopping in dense plasmas, Las. Int. Rel. Plasma P. H. 6 (1984) 1029−1048;
C. Deutsch, Inertial confinement fusion driven by intense ion Beams, Ann. Phys. Fr. 11 (1986) 1−111.

[38] F.I. McGuire, J.M. Peek, C.L. Pitchford, Proton stopping power of aluminium ions, Phys. Rev. A26 (1982) 1318−1325.

[39] S.P. Ahlen, Theoretical and experimental aspects of the energy loss of relativistic heavily ionizing particles, Rev. Mod. Phys. 52 (1980) 121−173.

[40] N. Bohr, The penetration of atomic particles through matter, Kgl. Dan. Vidensk. Selsk. Mat. Phys. Medd. 18 (1948) N8.

[41] G. Maynard, C. Deutsch, The Barkas effect or Z_P^3-contributions to stopping of swift charged particles, J. Phys. (Paris) 43 L (1982) 223−227.

[42] J.D. Jackson, R.L. McCarthy, Z_P^3 connection to energy loss and range, Phys. Rev. B6 (1972) 4131−4141;
J.C. Ashley, R.H. Ritchie, W. Brandt, Z_P^3 effect is stopping power of matter for charged particles, Phys. Rev. B5 (1972), 2393−2347;
K.W. Hill, E. Merzbacher, Z_P^3 effect in stopping power of matter for charged particles, Phys. Rev. A9 (1974) 156−165.

[43] C. Deutsch, S. Klarsfeld, Quadrupole electron broadening of neutral lines in a plasma, Phys. Rev. A7 (1973) 2081−2086.
[44] J. Lindhard, The Barkas effect or $Z_P^3 Z_P^4$ corrections to stopping of swift charged, Nucl. Instr. Meth. 132 (1976) 1−5.
[45] J. Lindhard, M. Scharff, H.E. Schioett, Range concepts and heavy ion ranges. Notes on atomic collisions II, Kgl. Dan. Vidensk. Selbsh. Mat. Fys. Medd. 33 (39) (1963) 1−42.
[46] X. Garbet, Charged Particle Stopping by Bound Electrons in a Plasma, Report L.P. N vol. 209, Université Paris XI, Orsay, 1984.
[47] H.H. Andersen, J.F. Ziegler, Stopping and Ranges of Ions in Matter, Pergamon, New-York, 1977.
[48] B. Tashev, F. Baimbetov, C. Deutsch, P. Fromy, Low velocity ion stopping in binary mixtures, Phys. Plasmas 15 (102701) (2008) 1−10.
[49] See for instance A. Ortner, A. Franck, A. Blazevic, M. Roth, Role of charge transfer in heavy-ion-beam-plasma interactions at intermediate energies, Phys. Rev. E91 (23104) (2015) 1−7.
[50] C. Deutsch, R. Popoff, Low ion-velocity slowing down in a strongly magnatized plasma target, Phys. Rev. E78 (56405) (2008) 1−8.
[51] C. Deutsch, N.A. Tahir, Fragmentation and stopping of heavy cluster ions in a lithium target-Application to target implosion, Phys. Fluids B4 (1992) 3735−3746;
N.A. Tahir, H.J. Lutz, O. Geb, J.A. Maruhn, C. Deutsch, et al., Inertial confinement fusion using hohlramm radiation generated by heavy ion cluster, Phys. Plasmas 4 (3) (1997) 796−816.
[52] Z. Wang, Bin He, Z.G. Fu, P. Zhang, Energy relaxation of multi-MeV protons travelling in compressed DT + Be plasmas, Phys. Plasmas 21 (72703) (2014) 1−4.
[53] H.B. Nersisyan, C. Deutsch, Stopping of ions in a plasma irradiated by an intense laser field, Laser Part. Beams 29 (2011) 389−397.
[54] B. Yu Sharkov, D.H.H. Hoffmann, A.A. Golubev, Y.T. Zhao, High energy density physics with intense ion beams, Matter Radiat. Extrem. 1 (2016) 28−47.
[55] J.A. Frenje, P.E. Grabowski, C.K. Li, F.H. Seguin, A.B. Zylstra, et al., Measurements of ion stopping around the Bragg peak in high-energy-density plasmas, Phys. Rev. Lett 115 (2015) 205001−205005.
[56] A.B. Zylstra, J.A. Frenje, P.E. Grabowski, C.K. Li, G.W. Collins, et al., Measurement of charged-particle stopping in warm dense plasma, Phys. Rev. Lett 114 (2015) 215002−215006.
[57] G. Maynard, C. Deutsch, Energy loss and straggling at any velocity of swift ions in dense matter, Phys. Rev. A26 (1982) 665−668;
Born RPA approximation for ion stopping in arbitrary degenerate electron fluid, J. de Physique 46 (1985) 1113−1123.
[58] S.N. Chen, C. Deutsch, S. Atzeni, M. Gauthier, J. Fuchs, EPS − 2015 Lisboa and to be published.